JGR Oceans

RESEARCH ARTICLE
10.1029/2025JC023770

Asymmetric Effects of Topographic Slopes and Bottom Friction on Lagrangian and Eulerian Eddy Diffusivities in Two-Layer QG Flow

Miriam F. Sterl[1,2], André Palóczy[3], J. H. LaCasce[4], Michiel L. J. Baatsen[2], and Sjoerd Groeskamp[1]

[1]Department of Ocean Systems, Royal Netherlands Institute for Sea Research, Texel, The Netherlands, [2]Institute for Marine and Atmospheric Research, Utrecht University, Utrecht, The Netherlands, [3]National Oceanography Centre, Liverpool, UK, [4]Department of Geosciences, University of Oslo, Oslo, Norway

Abstract We investigate how a topographic slope impacts eddy diffusivities in a two-layer quasi-geostrophic model. There are asymmetric effects of retrograde slopes, where the layer interface and the topography tilt in the same direction, and prograde slopes, where the interface and topography tilt in opposite directions. Moreover, there is asymmetry between the upper and lower layer. Steep retrograde slopes suppress the eddy diffusivity in both layers compared to flat or weak slopes. With a strong prograde slope, coherent, long-lived vortices form in the upper layer; as these are surface-trapped, they are not influenced by topography or bottom friction, and the diffusivity in the upper layer is thus relatively unaffected by the slope. In the lower layer, however, the diffusivities decrease with slope magnitude for both prograde and retrograde slopes. We also compare the Lagrangian diffusivity, derived from particle tracking experiments, and the Eulerian diffusivity, based on the flux-gradient relation for potential vorticity (PV). The two values agree in the upper layer, but not in the lower layer. We present a new expression relating Eulerian and Lagrangian diffusivities, and this correctly captures the differences seen in the lower layer. The difference occurs because bottom friction alters the PV along the particle tracks. The results underline the importance of considering both topographic slopes and bottom friction in parametrizations of mesoscale eddy stirring.

Plain Language Summary Ocean eddies mix properties such as heat, salt and nutrients, impacting oceanic ecosystems and climate. The strength of the mixing is expressed by the eddy diffusivity, measuring how much particles spread out in a flow. We study how the eddy diffusivity is impacted by a sloping seafloor. We use a model with two fluid layers, with a background flow in the upper layer and a sloping bottom in the lower layer. In the Northern Hemisphere, if the flow has the shallow side to its left, the eddy diffusivity gets weaker as the bottom slope gets steeper. If the flow has the shallow side to its right, the eddy diffusivity only gets weaker in the lower layer, but not in the upper. This is due to very strong eddies which form in the upper layer and are unaffected by the slope. We also evaluate an eddy diffusivity widely used in climate models. This matches the diffusivity determined from particles in the upper layer but not in the lower. We present a new relation which demonstrates that this difference stems from bottom friction. Thus, both the steepness and orientation of the slope and the bottom friction have important impacts on eddy mixing.

Key Points:

- In a two-layer QG model eddy diffusivity is suppressed over retrograde slopes in both layers, compared to a flat bottom case
- Over steep prograde slopes, long-lived, coherent, surface-trapped eddies form, and eddy diffusivity is suppressed only in the lower layer
- A relation between Lagrangian and Eulerian diffusivities is derived, showing that they differ in the lower layer due to bottom friction

Supporting Information:

Supporting Information may be found in the online version of this article.

Correspondence to:

M. F. Sterl,
miriam.sterl@mpimet.mpg.de

Citation:

Sterl, M. F., Palóczy, A., LaCasce, J. H., Baatsen, M. L. J., & Groeskamp, S. (2026). Asymmetric effects of topographic slopes and bottom friction on Lagrangian and Eulerian eddy diffusivities in two-layer QG flow. *Journal of Geophysical Research: Oceans*, *131*, e2025JC023770. https://doi.org/10.1029/2025JC023770

Received 18 NOV 2025
Accepted 26 MAR 2026

Author Contributions:

Conceptualization: Miriam F. Sterl, André Palóczy, J. H. LaCasce, Michiel L. J. Baatsen, Sjoerd Groeskamp
Formal analysis: Miriam F. Sterl, André Palóczy
Funding acquisition: Michiel L. J. Baatsen, Sjoerd Groeskamp
Methodology: Miriam F. Sterl, André Palóczy, J. H. LaCasce, Michiel L. J. Baatsen, Sjoerd Groeskamp
Software: Miriam F. Sterl, André Palóczy
Supervision: Michiel L. J. Baatsen, Sjoerd Groeskamp
Visualization: Miriam F. Sterl
Writing – original draft: Miriam F. Sterl, J. H. LaCasce

1. Introduction

Mesoscale eddies account for more than 90% of the surface kinetic energy in the oceans (Ferrari & Wunsch, 2009). They play a vital role in the ocean through the mixing of oceanic tracers such as heat, salt, carbon, oxygen, and nutrients (e.g., Lee et al., 2007; Gnanadesikan et al., 2013; Harrison et al., 2018; Jones & Abernathey, 2019; Ruan et al., 2023; Y. Zhang & Vallis, 2013). Eddies contribute to horizontal mixing in two different ways: by stirring tracers laterally and by trapping tracers in their cores and transporting them as they move (Abernathey & Haller, 2018; Denes et al., 2022; Frenger et al., 2015; W. Zhang & Wolfe, 2024; W. Zhang et al., 2020). In this study, we focus on horizontal eddy mixing through stirring. As most global ocean-climate models do not have sufficient horizontal resolution to explicitly resolve the mesoscale, which typically encompasses length scales of $\mathcal{O}(10-100)$ km, eddy mixing is usually parametrized (e.g., Eden & Greatbatch, 2008; Fox-Kemper et al., 2019; Gent & McWilliams, 1990; Hallberg, 2013; Hewitt et al., 2017, 2020; Jansen et al., 2015; Jansen & Held, 2014; Kjellsson & Zanna, 2017). One widely used approach to parametrize horizontal

Writing – review & editing:
André Palóczy, J. H. LaCasce, Michiel L. J. Baatsen, Sjoerd Groeskamp

eddy mixing through stirring is to relate the eddy-induced flux of a tracer, $\mathcal{F}_C$, to the background lateral tracer gradient ∇C via an eddy diffusivity, $\mathcal{K}$, following a Fickian flux-gradient relation:

$$\mathcal{F}_C = -\mathcal{K}\nabla C. \tag{1}$$

This parametrization assumes a scale separation between the background field and the eddy field, such that gridscale properties (∇C) can be used to infer subgridscale fluxes ($\mathcal{F}_C$). Climate models are highly sensitive to the eddy diffusivity ($\mathcal{K}$), which can have major consequences for the representation of global climate and ocean circulation (Chouksey et al., 2022; Gnanadesikan et al., 2015; Holmes et al., 2022; Pradal & Gnanadesikan, 2014). It is therefore vital to understand how $\mathcal{K}$ varies throughout the ocean and how it depends on external parameters in order to accurately parametrize it (Vallis, 2021).

One oceanic variable that can strongly modulate the eddy diffusivity is the slope of the seafloor, which varies significantly throughout the ocean (e.g., LaCasce, 2017). In regions of the ocean where the seafloor is steeply sloped, the diffusivity in the cross-slope direction is suppressed compared to the diffusivity in regions where the seafloor is flat (Isachsen, 2011). This suppression can be linked to a more general phenomenon: the suppression of eddy diffusivity by gradients in potential vorticity (PV), which act as a barrier for lateral transport and thus suppress diffusivity in the direction of the PV gradient (Balwada et al., 2016; Ferrari & Nikurashin, 2010; Griesel et al., 2015; Klocker, Ferrari, & LaCasce, 2012; LaCasce, 2000; Marshall et al., 2006; Nakamura & Zhu, 2010; O'Dwyer et al., 2000; Srinivasan & Young, 2014; Sterl et al., 2024). We will refer to this effect as PV suppression. Recent efforts have aimed to derive diagnostic expressions for the eddy diffusivity above topographic slopes (Brink, 2012, 2016; Brink & Cherian, 2013; Dettling et al., 2024, 2025; Nummelin & Isachsen, 2024; Wang & Stewart, 2020; Wei et al., 2022, 2024; Wei & Wang, 2021). Sterl et al. (2024) derived an analytical expression for eddy diffusivity as a function of topographic slope in a barotropic context. This predicted Lagrangian diffusivity compared favorably with depth-averaged diffusivities diagnosed from a numerical model using Equation 1. Despite the agreement, a shortcoming of this derivation is that it does not take into account baroclinic effects and vertical variations. The vertical structure of mesoscale eddies can have a significant baroclinic component and is influenced by topographic slope (e.g., De La Lama et al., 2016; Feng et al., 2021; LaCasce, 2017; LaCasce & Groeskamp, 2020; Ni et al., 2023; Steinberg et al., 2025; Yankovsky et al., 2022). Moreover, estimates of eddy diffusivity all show variations with depth (Zika & McDougall, 2008; Zika et al., 2010; Cole et al., 2015; Chapman & Sallée, 2017; Groeskamp et al., 2017, 2020, W. Zhang & Wolfe, 2022). Therefore, the first goal of the present study is to better understand how topographic slopes affect eddy diffusivity throughout the water column.

To move our study of eddy diffusivity from a barotropic to a baroclinic framework, we use the two-layer quasi-geostrophic (2LQG) model (Phillips, 1951, 1954). The model consists of a layer of lighter fluid on top of a layer of denser fluid. The layers have different background flows (typically zonal), and the vertical shear can make the flow baroclinically unstable. The 2LQG model is the simplest model of stratification and baroclinic instability (Flierl, 1978), the main generation mechanism of mesoscale eddies (e.g., Gill et al., 1974; Robinson & McWilliams, 1974). Thus, due to its simplicity and incorporation of crucial features of baroclinic flows, the 2LQG model is widely used to study eddy fluxes and diffusivities.

Typically, eddy diffusivity in the 2LQG model is derived from the flux-gradient relation (1) using the baroclinic eddy streamfunction as a tracer and assuming it is advected by the barotropic flow (Larichev & Held, 1995; Salmon, 1980). In the QG framework, the baroclinic streamfunction is directly proportional to the height of the isopycnal interface between the two layers. As such, a positive (negative) baroclinic streamfunction corresponds to a locally deeper (shallower) upper layer, meaning that in a depth-averaged sense, the fluid is lighter (denser) here. The baroclinic streamfunction can thus be seen as the local density or (inverse) temperature anomaly with respect to the background state. Multiple studies have derived scalings or parametrizations for the diffusivity based on the baroclinic streamfunction; this was done for the flat bottom f-plane case by Thompson and Young (2006), Gallet and Ferrari (2020) and Chen (2023), and for the flat bottom β-plane case by Thompson and Young (2007), Gallet and Ferrari (2021) and Chang and Held (2021). Their findings were extended by Deng and Wang (2024) to sloping topography (on an f-plane). In line with PV suppression, it was found that the eddy diffusivity decreases as planetary or topographic PV gradients increase (Deng & Wang, 2024; Gallet & Ferrari, 2021; Thompson & Young, 2007). The dependence of the diffusivity on the orientation of the topographic slope was also studied by Deng and Wang (2024), considering two relative orientations: retrograde (prograde) topographic slopes tilt in the same (opposite) direction as the isopycnal interface (e.g., Pavec et al., 2005; Sterl

et al., 2025). Both slopes suppress mixing, but there is an asymmetry between them, depending on the bottom drag: diffusivities are higher for prograde (retrograde) slopes in a regime of weak (strong) bottom drag. Recently, Pudig and Smith (2025) demonstrated that diffusivities are also suppressed over rough bathymetry, making a sudden transition when the topographic heights exceed a critical value.

In most of these studies, the focus was on advection of the baroclinic streamfunction by the barotropic flow, yielding a single diffusivity. As we are interested in the vertical structure of diffusivity, we will differentiate between the values obtained in the layers. These can be quite different over a sloping bottom. Diffusivities are usually estimated from eddy fluxes, an Eulerian approach. Diffusivities in the ocean on the other hand are generally computed using Lagrangian methods, following Taylor (1921) (see Davis, 1987; Davis, 1991; LaCasce, 2008a). Lagrangian methods include the use of surface drifters (Chiswell, 2013; Colin de Verdiere, 1983; Davis, 1991; Zhurbas et al., 2014; Zhurbas & Oh, 2003, 2004), subsurface floats (Balwada et al., 2016; Freeland et al., 1975; LaCasce et al., 2014), numerical particle tracking (Griesel et al., 2010; Klocker, Ferrari, Lacasce, & Merrifield, 2012), or combinations thereof (Oelerich et al., 2025; Roach et al., 2018; Rühs et al., 2018; Rypina et al., 2012). In the 2LQG model, particle tracking can be used to calculate layer-wise diffusivities. But a question arises: how well do Lagrangian and Eulerian diffusivities compare? This was studied by W. Zhang et al. (2020) and W. Zhang and Wolfe (2024) for the flat bottom β-plane case. They found good agreement between the two approaches. However, they only made the comparison for the upper layer. Thus a second goal of this study is to determine how well the Eulerian and Lagrangian diffusivities match throughout the water column, for varying topographic PV gradients.

To this end, we run numerical simulations of the 2LQG model with varying topographic slopes, and diagnose both Lagrangian and Eulerian diffusivities in both layers. We find there is an asymmetric effect of prograde and retrograde slopes, especially in the upper layer. Retrograde slopes suppress the Lagrangian diffusivity in both layers, in line with expectations. In contrast, over prograde slopes, coherent, surface-trapped eddies form that are not affected by bottom effects. As such, the Lagrangian diffusivity is not suppressed in the upper layer (though it is in the lower layer). We also find that while the Eulerian and Lagrangian diffusivities match in the upper layer, they differ in the lower layer. We show that this is due to bottom friction, and derive an analytical expression relating the Eulerian and Lagrangian diffusivities. Our results highlight the importance of considering topographic slopes as well as bottom friction when studying and parametrizing mesoscale eddy stirring.

The manuscript is organized as follows. In Section 2, we review the 2LQG model equations, describe the numerical models we use, and discuss Lagrangian and Eulerian approaches of diagnosing eddy diffusivity from our simulations. Section 3 discusses the Lagrangian and Eulerian flow field characteristics and eddy diffusivities, and presents the analytical relation between the two diffusivity measures. We end with a summary and discussion in Section 4.

2. Methods

2.1. Model Equations

We consider the 2LQG model on an f-plane with a rigid lid over a linear bottom slope α in the y-direction. We choose an f-plane in order to focus on the effect of topographic PV without having to consider the effects of planetary PV (Deng & Wang, 2024). We index the upper layer with $j = 1$ and the lower layer with $j = 2$. The two layers have densities ρ_j and thicknesses H_j, and thus the deformation radius in layer j is given by

$$\lambda_j = \frac{\sqrt{g' H_j}}{f_0}, \tag{2}$$

with f_0 the Coriolis parameter and $g' = g(\rho_2 - \rho_1)/\rho_2$ the reduced gravity. The flow field is split into a stationary background field and a perturbation to that background field, which we refer to as the eddy field. We prescribe a zonal background flow U in the upper layer and no background flow in the lower layer. The background PV per layer is denoted by Q_j and is equal to the sum of the stretching PV and topographic PV:

$$Q_1 = F_1 U y, \tag{3a}$$

$$Q_2 = \left(-F_2 U + \frac{f_0}{H_2}\alpha\right) y, \tag{3b}$$

with $F_j \equiv 1/\lambda_j^2$. From (3b), there exists a critical topographic slope at which the lower layer PV gradient vanishes: $\alpha_c = f_0 U / g'$. In the frictionless case, α_c is the critical slope for instability (Charney & Stern, 1962; Pavec et al., 2005; Pedlosky, 1963, 1964; Steinsaltz, 1987; Tang, 1976), but linear bottom friction destabilizes the system even beyond α_c (Sterl et al., 2025). The eddy PV q_j and the eddy velocities $\mathbf{u}_j$ are related to the eddy streamfunctions ψ_j:

$$q_j = \nabla^2 \psi_j + (-1)^j F_j (\psi_1 - \psi_2), \tag{4a}$$

$$\mathbf{u}_j = (u_j, v_j) = \left(\frac{-\partial \psi_j}{\partial y}, \frac{\partial \psi_j}{\partial x}\right). \tag{4b}$$

In the lower layer, we employ linear bottom friction with a frictional timescale of μ^{-1}, acting as an energy sink to balance the energy input by baroclinic instability. The evolution equations for the eddy streamfunctions then become

$$\frac{\partial q_1}{\partial t} + U\frac{\partial q_1}{\partial x} + F_1 U \frac{\partial \psi_1}{\partial x} + \mathcal{J}(\psi_1, q_1) = 0, \tag{5a}$$

$$\frac{\partial q_2}{\partial t} + \left(-F_2 U + \frac{f_0 \alpha}{H_2}\right)\frac{\partial \psi_2}{\partial x} + \mathcal{J}(\psi_2, q_2) = -\mu \nabla^2 \psi_2, \tag{5b}$$

where $\mathcal{J}(a,b) = \frac{\partial a}{\partial x}\frac{\partial b}{\partial y} - \frac{\partial a}{\partial y}\frac{\partial b}{\partial x}$ is the Jacobian operator.

2.2. Simulating Flow Fields

To simulate 2LQG flow governed by Equations 5a and 5b, we use GeophysicalFlows.jl (Constantinou et al., 2021), which solves the QG equations on square, doubly periodic domains using Fourier-based pseudo-spectral methods. A filtered fourth-order Runge-Kutta timestepping scheme is used. The filter removes enstrophy at high wavenumbers at every time step (no explicit lateral viscosity was applied, so a small part of the high-wavenumber energy also ends up in the filter). All simulation parameters are listed in Table 1. We employ a flat bottom as well as a range of positive and negative topographic slopes, keeping all other parameters constant. Here a positive slope means the bottom is sloping toward the north. We apply a positive zonal shear and a positive Coriolis parameter, so positive slopes are retrograde and negative slopes are prograde in our simulations. The slopes cover a range between $\pm 7 \times 10^{-3}$; the corresponding non-dimensionalized topographic PV gradients, $\left(f_0 \alpha / H_2\right) \cdot \lambda_2^2 / U$, cover a range between ± 1.34. Stratification and flow in the ocean are surface-intensified, and we therefore consider different layer thicknesses for the upper and lower layer. We employ an eastward background flow in the upper layer of 0.2 m s^{-1} and linear bottom friction with an inverse frictional timescale of 3×10^{-6} s^{-1}; the non-dimensionalized friction, $\mu \cdot \lambda_2 / U$, is 0.59. The parameter values are chosen in such a way that eddy velocities are of order 10 cm/s—realistic for the ocean (e.g., Naveira Garabato et al., 2011)—for steep slopes, while the flow reaches a statistically steady state for most of the tested slope values. Only the cases with slopes $\alpha = -5 \times 10^{-3}$ and $\alpha = -7 \times 10^{-3}$ do not reach statistical equilibrium by the end of the simulations, as will be further discussed in Section 3.1. Every simulation is initialized with a random eddy PV field of magnitude q_0, spun up to equilibrium for 1,000 model days, after which the output is saved for 670 model days. To check if the results are robust to changing initial conditions, we simulate three realizations for each slope, each with a different random seed to initialize the PV; we refer to these as R1, R2, and R3. Note that if the results are indeed robust to initial conditions, this approach should be equivalent to running one longer simulation.

2.3. Particle Tracking

We use Parcels (Delandmeter & van Sebille, 2019) to advect virtual particles. For each realization, we perform an ensemble of 10 particle releases, released at intervals of 30 days. The particles start from a uniform distribution

Table 1
Model Parameters for the GeophysicalFlows.jl Simulations

Quantity	Symbol	Value
Number of grid points	n	256
Domain size	L	700 km
Horizontal grid size	Δx	2.7 km
Simulation timestep	Δt	200 s
Output timestep	Δt_{out}	1 hr
Coriolis parameter	f_0	10^{-4} s^{-1}
Planetary PV gradient	β	0
Height upper layer	H_1	1,000 m
Height lower layer	H_2	4,000 m
Gravitational acceleration	g	9.81 m s^{-2}
Density upper layer	ρ_1	1,027.6 kg m^{-3}
Density lower layer	ρ_2	1,028 kg m^{-3}
Deformation radius upper layer	λ_1	20 km
Deformation radius lower layer	λ_2	39 km
Bottom friction	μ	3×10^{-6} s^{-1}
Zonal background flow upper layer	U	0.2 m s^{-1}
Magnitude of initial eddy PV field	q_0	3×10^{-6} s^{-1}
Topographic slope	α	$[0, 1, 2, 3, 5, 7] \times [10^{-4}, 10^{-3}]$
Critical topographic slope	α_c	5.24×10^{-3}

across the domain and are advected using a fourth-order Runge-Kutta advection scheme. Parcels linearly interpolates the velocities in space and time. We save time series of particle locations and velocities along the particle trajectories. The particle tracking is performed separately for each layer. The simulation settings are listed in Table 2.

2.4. Calculating Eddy Diffusivity

2.4.1. Lagrangian Diffusivity

We compute the Lagrangian eddy diffusivity from the particle trajectories. The cross-stream Lagrangian eddy diffusivity $\mathcal{K}_L$ is defined as one-half the derivative of the cross-stream dispersion, which is the mean squared cross-stream displacement from the starting y-coordinate, y_0 (Taylor, 1921) (Note in our simulations the cross-stream direction is cross-slope, and the two terms can be used interchangeably.) The diffusivity can be rewritten in a number of ways (Davis, 1991; LaCasce, 2008a; LaCasce et al., 2014; Taylor, 1921):

$$\mathcal{K}_{L,j}(t) \equiv \frac{1}{2}\frac{\mathrm{d}}{\mathrm{d}t}\left\langle \left[y_j(t) - y_j(0)\right]^2 \right\rangle_L \tag{6a}$$

$$= \left\langle v_j(t)\left[y_j(t) - y_j(0)\right] \right\rangle_L \tag{6b}$$

$$= \left\langle v_j(t) \int_0^t v_j(t')dt' \right\rangle_L \tag{6c}$$

$$= \int_0^t \langle v_j(t) v_j(t') \rangle_L \mathrm{d}t' \tag{6d}$$

$$\equiv \nu_j^2 T_{L,j}. \tag{6e}$$

Table 2
Parameters for the Parcels Simulations

Variable	Value
Number of particle releases	10
Number of particles per release	400
Time between releases	30 days
Duration of each release	400 days
Advection timestep	1 hr
Output timestep	12 hr

The brackets $\langle\cdot\rangle_L$ denote the average over all particles, and the subscript j is the layer index. In (6d) the cross-stream diffusivity is expressed as the integral of the cross-stream velocity autocovariance. If the velocity is statistically stationary, the autocovariance can be normalized by factoring out the velocity variance ν^2. Note that ν^2 is equal to the velocity autocovariance at lag 0, or, equivalently, to the time-averaged cross-stream eddy kinetic energy (EKE). The eddy diffusivity is then equal to ν^2 times the integral of the velocity autocorrelation, the Lagrangian integral timescale T_L. This is a measure of the predictability time for the system.

Due to PV suppression, the eddies spread preferentially in the zonal direction. Particles first spread out in the meridional direction due to the swirling motion of the eddies, but then move back toward their starting latitudes. Thus the cross-stream velocity autocovariance becomes negative before it converges to zero as the memory of the system runs out. As a result, $\mathcal{K}_L$ and T_L usually have an initial peak, then decrease and converge as $t \to \infty$ (Balwada et al., 2016; Griesel et al., 2015; LaCasce et al., 2014; Zhurbas et al., 2014). We focus solely on the asymptotic values of $\mathcal{K}_L$ and T_L.

For each particle release, we compute time series of the cross-stream velocity autocovariance averaged over all particles. We employ the biased autocovariance, to smooth the time series for large time lags. We use (6d) to compute time series of diffusivity, using the trapezoidal rule for the integral of the autocovariance. We normalize the diffusivity by the autocovariance at lag 0 to obtain the Lagrangian integral timescale (Equation 6e). We have 3 flow field realizations and 10 particle releases per flow field for each topographic slope, resulting in 30 time series of T_L and $\mathcal{K}_L$ for each slope. Limit values of T_L and $\mathcal{K}_L$ are computed as the mean over those 30 time series over the last 100 days of each particle release.

2.4.2. Eulerian Diffusivity

To compute the Eulerian cross-stream eddy diffusivity $\mathcal{K}_E$, we use the flux-gradient relation (1) with PV as a tracer:

$$\langle v_j q_j \rangle_E = -\mathcal{K}_{E,j} \frac{\partial Q_j}{\partial y}, \tag{7}$$

where $\langle\cdot\rangle_E$ denotes the area average. The asymptotic values of $\mathcal{K}_E$ are computed as the mean over the 3 flow field realizations per slope, over the whole equilibrated time series of 670 days. The layer diffusivities are related, as the vertically summed PV fluxes must vanish following Bretherton's relation (Bretherton, 1966):

$$\delta_1 \langle v_1 q_1 \rangle_E + \delta_2 \langle v_2 q_2 \rangle_E = 0. \tag{8}$$

Here $\delta_j \equiv H_j/H$ are the layer depth ratios and $F \equiv \delta_1 F_1 = \delta_2 F_2$. This in turn has implications for the diffusivities. With a flat bottom, the mean PV gradients are:

$$\frac{\partial Q_1}{\partial y} = F_1 U, \quad \frac{\partial Q_2}{\partial y} = -F_2 U. \tag{9}$$

Using these and the diffusivities (7) in the Bretherton relation yields:

$$\delta_1 \mathcal{K}_{E,1} F_1 U - \delta_2 \mathcal{K}_{E,2} F_2 U = 0 \quad \rightarrow \quad \mathcal{K}_{E,1} = \mathcal{K}_{E,2}. \tag{10}$$

The layer diffusivities over a flat bottom are equal, regardless of the layer depths. However, this is no longer true with a bottom slope. With the PV gradient from (3b), we obtain:

$$\frac{\mathcal{K}_{E,2}}{\mathcal{K}_{E,1}} = \frac{1}{1 - \alpha/\alpha_c}, \tag{11}$$

with $\alpha_c = f_0 U/g'$ the critical slope. Thus the bottom diffusivities are larger than at the surface for positive slopes and smaller for negative slopes. Moreover, if the slope exceeds the critical slope, one of the diffusivities must be negative.

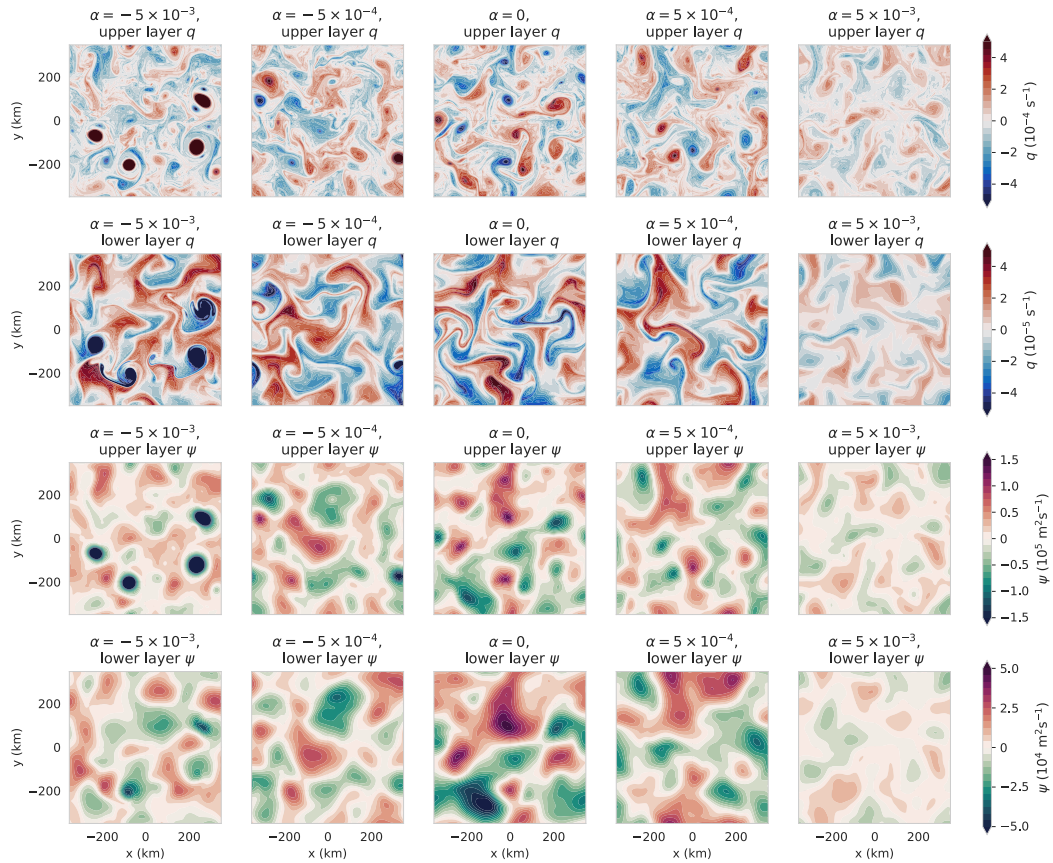

Figure 1. Snapshots of eddy potential vorticity and streamfunction fields from the R1 flow realizations in the upper layer (first row) and lower layer (second row) for different bottom slopes α. Note the different magnitudes on the colorbars for the upper and lower layer.

The lower layer PV fluxes, and hence the deep diffusivities, are related to the deep kinetic energy (Larichev & Held, 1995; Thompson & Young, 2006). This follows from the equation for the total energy, which yields a balance between baroclinic production and dissipation in the bottom Ekman layer in a statistical steady state (e.g., Thompson & Young, 2007). Thus, with the Bretherton relation (8):

$$\langle v_2 q_2 \rangle_E = -\frac{\delta_1}{\delta_2} \langle v_1 q_1 \rangle_E = \frac{2\mu}{\delta_2 U} \mathrm{EKE}_2, \tag{12}$$

where

$$\mathrm{EKE}_2 = \frac{\delta_2}{2} \langle |\nabla \psi_2|^2 \rangle_E. \tag{13}$$

This relation holds regardless of topographic slope (as the topographic term vanishes in the energy equation).

3. Results

3.1. Eddy Flow Fields, Energies and Fluxes From Simulations

Figure 1 shows snapshots of the eddy PV and streamfunction fields from the R1 flow realizations for 5 different bottom slopes: a flat bottom, a weak positive and negative slope and a strong positive and negative slope (Movies showing the evolution of the eddy PV field and the movement of the particles can be found in the Supporting Information S1.) The eddy fields are highly isotropic (i.e., no jets form, due to the strong bottom friction; Vallis &

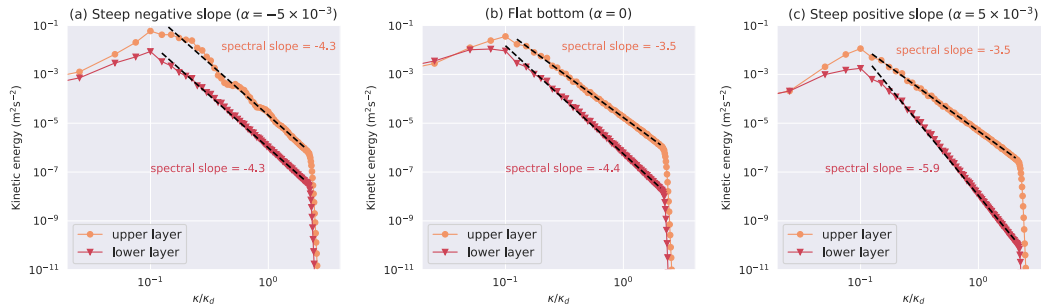

Figure 2. Spectra of the layer eddy kinetic energies $\frac{1}{2}\frac{H_j}{H}|\nabla\psi_j|^2$ as a function of wavenumber magnitude, for different topographic slopes α. Results are averaged over all output times of the GeophysicalFlows.jl runs and over the three flow field realizations. On the horizontal axis, the wavenumber magnitude is normalized by the baroclinic deformation wavenumber $\kappa_d = \sqrt{F_1 + F_2}$. The black dashed lines show the spectral slopes.

Maltrud, 1993; Kong & Jansen, 2017) and are surface-intensified. The eddy PV reveals more coherent vortices in the upper layer than in the lower layer, where there is more filamentation. The size of the eddies does not appear to change with the topographic slope magnitude or orientation. This is also seen in the energy spectra (Figure 2): the peak wavenumbers of the kinetic energy spectra are not impacted by the topographic slope. The peak energy scale is always at a quarter of the domain scale. The spectral slopes are steeper than -3, which represents an enstrophy cascade (Kraichnan, 1967), due to the filter removing enstrophy at high wavenumbers. Moreover, the spectral slopes are steeper in the lower layer than in the upper because bottom friction removes enstrophy at all scales. As such, there is less enstrophy to transfer to successively larger wavenumbers in the inertial range. The lower layer spectral slope is steepest for a positive slope.

The snapshots of q and ψ in Figure 1 reveal different aspects for the positive and negative slopes. The eddies over weak positive or negative slopes look similar to the flat bottom case. For a steep positive slope, the eddies are weaker. In contrast, with a steep negative slope ($\alpha = -5 \times 10^{-3}$ in the figures), something interesting happens: long-lived coherent vortices with much stronger PV and streamfunction anomalies emerge in the upper layer. The strong streamfunction signature is absent in the lower layer, indicating that the vortices are surface-trapped. As such, they are only weakly affected by bottom friction, and are thus strong and persistent. The high PV is visible in both layers, although in the lower layer the PV is filamented like the rest of the PV field.

These "monster eddies" appear in all runs with a negative topographic slope steeper than $\alpha = -1 \times 10^{-3}$, and increase in intensity as the slope steepens. Their imprint is clearly visible in the kurtosis of the eddy PV q, shown in Figure 3: the kurtosis becomes very large for steep negative slopes. Similar long-lived, surface-trapped vortices were found previously in 2LQG flat bottom β-plane simulations with a westward mean flow by Arbic and Flierl (2004b) and Berloff et al. (2011). We return to this later on.

Monster eddies can trap particles in their cores. This complicates calculating Lagrangian diffusivities because the trapped particles can be transported over large distances, rather than advected randomly with the fluid between vortices. Tracking trapped particles thus yields information about the vortex motion rather than the diffusive mixing (Abernathey & Haller, 2018; LaCasce, 2008b; W. Zhang et al., 2020; W. Zhang & Wolfe, 2024). Once a particle is trapped in a monster eddy, its velocity is correlated over long periods and the Lagrangian integral timescale and eddy diffusivity no longer converge. Therefore, we exclude trapped particles in the subsequent analyses.

We identify the trapped particles as follows. For each release, we examine the flow field and particle locations at the final time step of the particle advection. We compute the spatial mean and standard deviation of this final eddy PV field. We then remove particles at locations where q is more than 2.5 standard deviations from the mean. We apply this procedure only to the upper layer, as the monster eddies are surface-trapped. On average, around 2% of the particles are removed in the runs without monster eddies, while up to 8% of the particles are removed in the monster eddy runs. This filtering leads to differences in the average diffusivity of less than 8% for the runs without monster eddies, but up to 80% for the runs with monster eddies (see Figures S1 and S2 in Supporting Information S1). Figure 4 shows a snapshot of the upper layer eddy PV and EKE fields overlaid with the particle

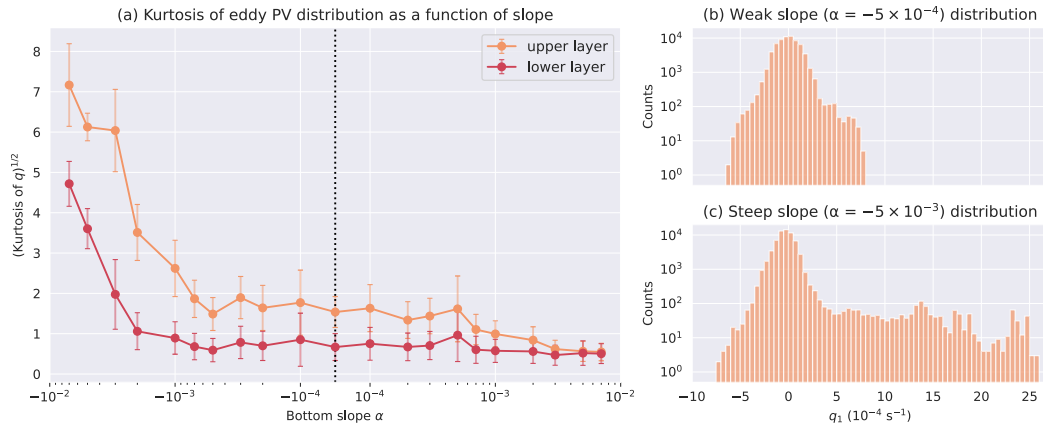

Figure 3. (a) Square root of the kurtosis of the Eulerian distribution of q as a function of the topographic slope. The points are the averages and the error bars are the standard deviations over the last 100 days of the R1, R2, and R3 flow realizations. (b), (c) Histograms showing the distribution of the upper layer eddy potential vorticity field at the last time step of the R1 flow realization for a weak negative slope and a steep negative slope, respectively.

locations for a simulation that contains monster eddies. Particles that are filtered out are indicated in white. Note that a few of the monster eddies have anomalously high EKE around the core. Particles trapped in the core experience anomalously low EKE.

The cases with slopes $\alpha = -5 \times 10^{-3}$ and $\alpha = -7 \times 10^{-3}$ are not in statistical equilibrium by the end of the simulations. This is due to the continued growth of the monster eddies. As such, the simulations eventually become numerically unstable. Thus a statistical description of these flow fields is not sensible, and we exclude these cases from our analyses.

Figure 5 shows the cross-stream eddy PV fluxes $\langle v_j q_j \rangle$ and the cross-stream eddy kinetic energies $\langle v_j^2 \rangle$ across all simulated slopes. For comparison, both the Lagrangian (averaged over all particles) and Eulerian (averaged over all grid points) values are shown. The fluxes follow the same trends in both layers but with different signs and magnitudes, following the Bretherton relation (8). There is a strong asymmetry between steep positive and negative topographic slopes. For steep positive slopes, the PV fluxes are suppressed compared to the flat bottom case, as expected from stability considerations. For steep negative slopes, however, the fluxes are comparable to those with a flat bottom, and vary little with slope. In the upper layer, the Lagrangian fluxes fluctuate strongly in time, but the time-averaged Lagrangian and Eulerian PV fluxes match for all slopes in both layers.

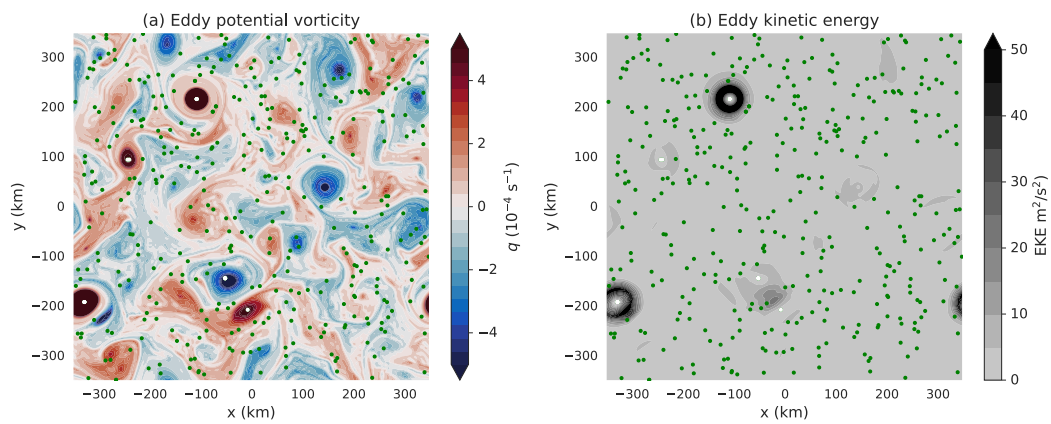

Figure 4. Snapshot of the eddy potential vorticity and eddy kinetic energy fields in the upper layer of the R1 flow field realization with slope $\alpha = -3 \times 10^{-3}$. The locations of the particles in the flow fields are indicated in green. Particles that are excluded from the analysis are indicated in white.

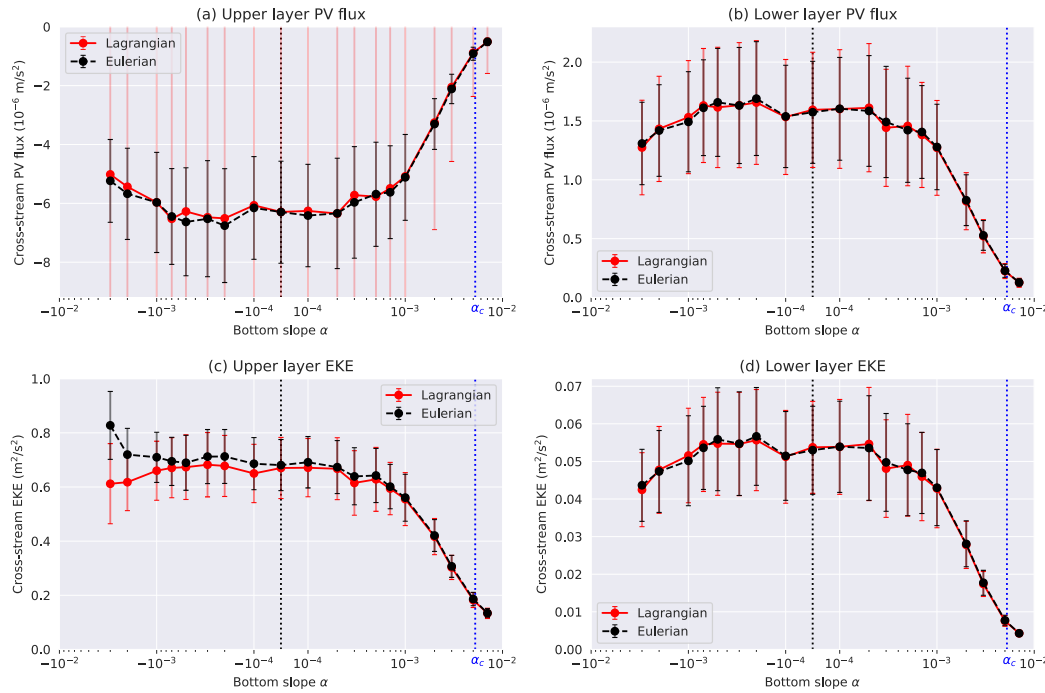

Figure 5. Lagrangian and Eulerian cross-slope eddy potential vorticity fluxes $\langle v_j q_j \rangle$ (a), (b) and cross-slope eddy kinetic energy $\langle v_j^2 \rangle$ (c), (d) as a function of the topographic slope. For the Eulerian values, the points are the averages and the error bars are the standard deviations over the full equilibrated time series of the R1, R2, and R3 flow realizations. For the Lagrangian values, the averages and standard deviations are over the full timeseries of all particle releases of the three flow realizations. The critical slope $\alpha_c = f_0 U/g'$ is indicated with the blue dotted line.

The same behavior is seen in the cross-stream EKE. As the flows are isotropic, the along-stream EKE is almost the same (not shown). The lower layer EKE follows the exact same trend as the PV fluxes due to the linear relation (12). The upper layer EKE is very similar, though an order of magnitude larger, as follows from linear stability analysis: the amplitude of the upper layer streamfunction is stronger (e.g., Pedlosky, 1987) (There is also some effect of the difference in layer thickness; equal layer thicknesses reduce the ratio between the upper and lower layer EKE, though the EKE remains higher in the upper layer.) The Lagrangian and Eulerian EKE values match in all cases within the variability ranges. Differences seen with steep negative slopes are caused by the monster eddies; their anomalously high EKE is not sampled by the particles (Figure 4), but is captured in the Eulerian EKE.

3.2. Eddy Diffusivities

We now turn our attention to the cross-slope eddy diffusivities, starting with the Lagrangian diffusivities. Time series of Lagrangian diffusivities are shown for three different slopes in Figure 6. As described in Section 2.4.1, the timeseries have an initial peak, after which the diffusivity converges. In the upper layer, the limit value of the diffusivity is the same for a steep negative slope and a flat bottom, but it is less over a steep positive slope. Note that with $\alpha = -3 \times 10^{-3}$ there are three lines that don't converge; here not all trapped particles were captured by our filter. However, we still find a converging timeseries for the mean of all runs. In the lower layer, the diffusivities and the variations between realizations and particle releases are reduced over both steep negative and positive slopes.

Figure 7 shows the limit diffusivities for all slopes. Both Lagrangian and Eulerian diffusivities are shown, but for the moment we focus on the Lagrangian values (red line). The upper layer diffusivity follows the same trend as the eddy PV fluxes and EKE: the values are unaffected by negative topographic slopes, but are suppressed over steep positive slopes. The variations between realizations and particle releases are also smaller for positive slopes. The

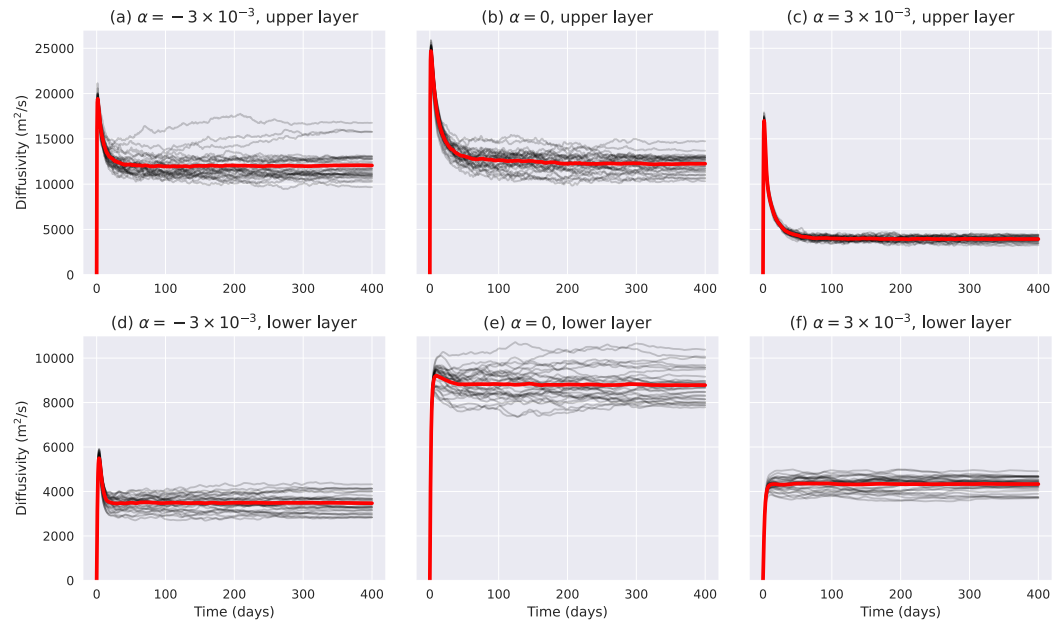

Figure 6. Time series of the Lagrangian cross-slope eddy diffusivity in the upper and lower layer for different topographic slopes α. Each individual black line shows one particle release in one of the flow field realizations. The red line shows the average over all flow field realizations and particle releases.

lower layer, however, shows very different behavior: here the diffusivities decrease for both positive and negative slopes. The suppression is somewhat greater with positive slopes.

For almost all slopes, the diffusivity is lower in the lower layer than in the upper layer. This is also the case with a flat bottom; here the average ratio of lower-to-upper layer diffusivity is 0.72 (Figure 7c), contrary to the expectation that the layer diffusivities are equal over a flat bottom (Equation 10). Topographic slopes have a clear impact on the lower-to-upper layer diffusivity ratio, and again, there is a strong asymmetry between positive and negative slopes. Going from negative to positive slopes, the ratio increases almost monotonically, and even becomes larger than 1 for $\alpha \in [2,3] \times 10^{-3}$. For steeper positive slopes, the ratio drops back to values closer to the flat bottom ratio.

The ratio of the Lagrangian diffusivity and the Lagrangian cross-stream EKE gives the Lagrangian integral timescale, T_L (Equation 6e), shown in Figure 8. As the upper layer diffusivity and EKE follow the same trend, so does T_L: it is lower over positive than over negative slopes. In the lower layer, the behavior of T_L is exactly opposite: it increases almost monotonically from negative to positive slopes, decreasing eventually for steep positive slopes. This trend is the same as that of the lower-to-upper layer diffusivity ratio (Figure 7c). Note, again, the difference in the order of magnitude between the two layers. In the upper layer, T_L is on the order of a few hours, whereas in the lower layer it is on the order of days.

Now we consider the Eulerian diffusivity, computed as the cross-slope eddy PV flux divided by the background PV gradient (Equation 7). The Eulerian diffusivity is shown in black in Figure 7. It has larger error bars than the Lagrangian diffusivity in both layers, indicating larger variation between realizations. In the upper layer (Figure 7a), the diffusivities agree well, as found previously by W. Zhang et al. (2020) and W. Zhang and Wolfe (2024). Only for steep negative slopes—the simulations with monster eddies—are the Lagrangian diffusivities higher than the Eulerian values, albeit with overlapping error bars.

In the lower layer (Figure 7b), up to a slope of $\alpha = 2 \times 10^{-3}$ the Lagrangian and Eulerian diffusivities follow a similar trend with slope, but the Eulerian value is consistently larger than the Lagrangian. This offset exists even for a flat bottom, so it is not caused by topographic slopes. With $\alpha = 5 \times 10^{-3}$, the Eulerian diffusivity is approximately 38,000 m^2/s (this data point falls outside the axis range in Figure 7b), as this slope is very close to the critical slope α_c (Section 2.1); here the Eulerian PV diffusivity becomes ill-defined. Then, for a slope of

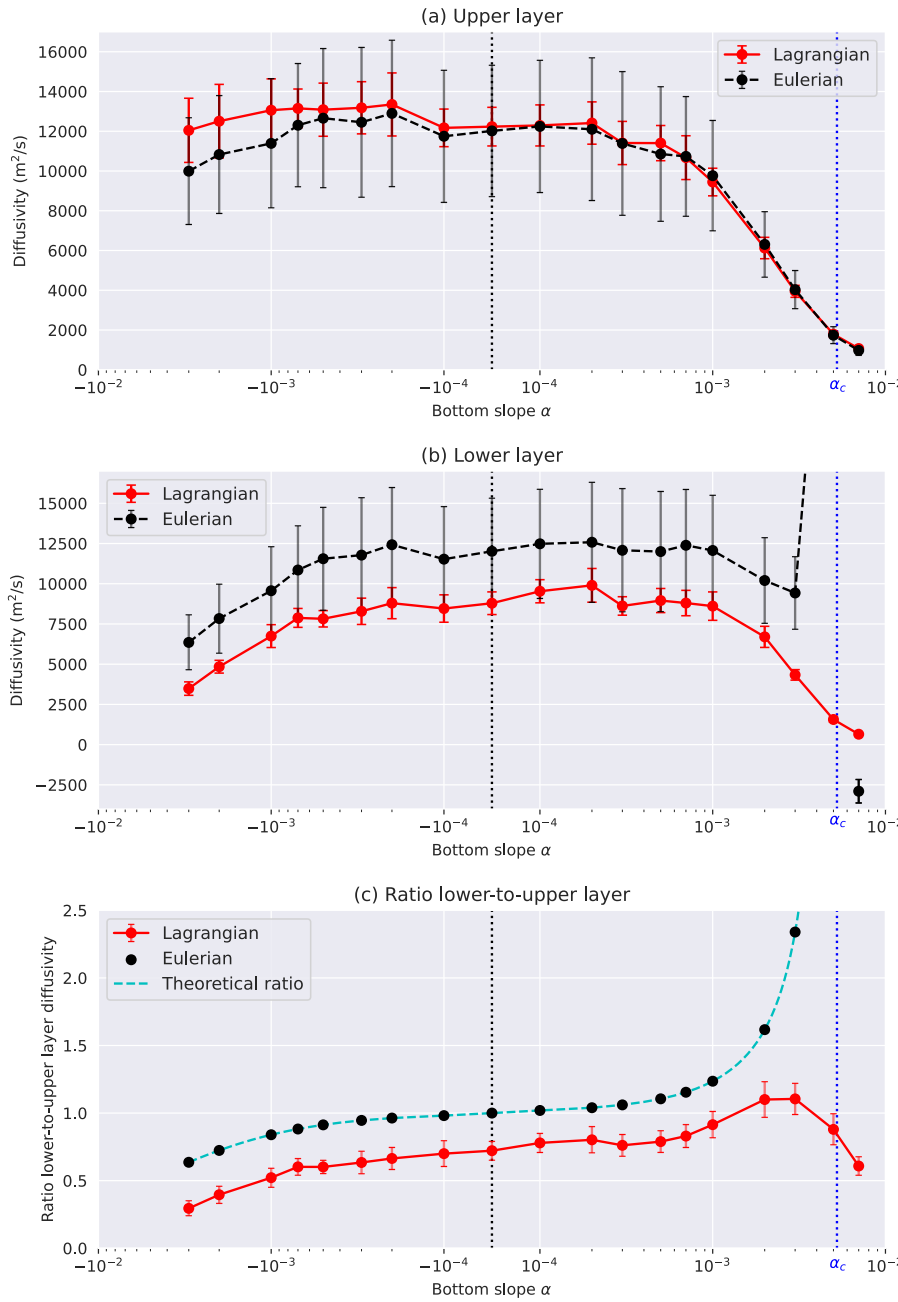

Figure 7. Lagrangian and Eulerian cross-slope diffusivities as a function of the topographic slope. The points are the averages and the error bars are the standard deviations over the R1, R2, and R3 flow realizations; for the Eulerian diffusivities over the full 670 days of the equilibrated flow fields, for the Lagrangian diffusivities over the last 100 days of each particle release. The critical slope $\alpha_c = f_0 U/g'$ is indicated with the blue dotted line. The theoretical lower-to-upper layer ratio plotted in (c) is defined in Equation 11.

$\alpha = 7 \times 10^{-3}$, the Eulerian diffusivity becomes negative as the lower layer PV gradient switches from negative to positive for slopes larger than α_c, while the lower layer PV flux remains positive for all slopes (Figure 5). This implies an up-gradient eddy PV flux.

The theoretical ratio of the lower and upper layer Eulerian diffusivity (Equation 11) is plotted in Figure 7c. The Eulerian ratios fall onto this curve. The ratio is equal to one for a flat bottom; for a negative slope, the diffusivity is largest in the upper layer, and for a positive slope it is largest in the lower layer. Up to a slope of $\alpha = 2 \times 10^{-3}$,

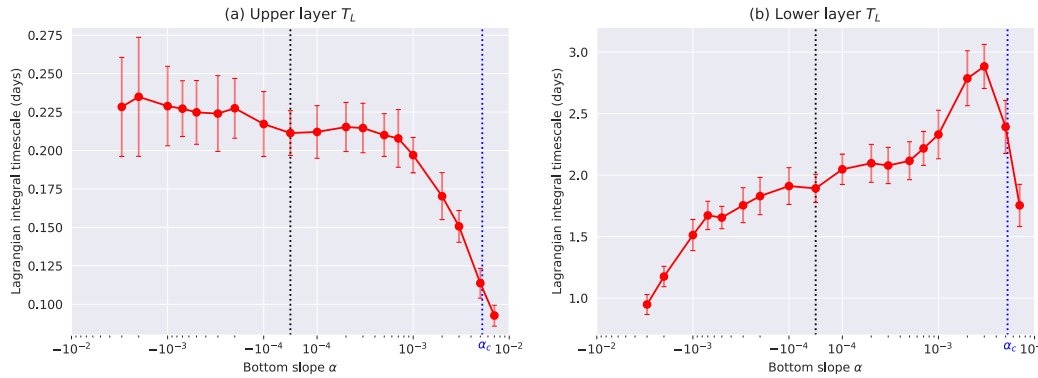

Figure 8. Lagrangian integral timescale (computed as the ratio of the cross-slope Lagrangian diffusivity and cross-slope Lagrangian eddy kinetic energy) as a function of the topographic slope. The points are the averages and the error bars are the standard deviations over the last 100 days of the R1, R2, and R3 flow realizations. The critical slope $\alpha_c = f_0 U/g'$ is indicated with the blue dotted line.

the Lagrangian ratio follows the trend as the Eulerian ratio, increasing with the topographic slope, but consistently lower. The Eulerian ratio diverges as $\alpha \to \alpha_c$, and becomes negative for $\alpha > \alpha_c$, whereas the Lagrangian ratio remains positive and decreases.

3.3. Frictional Modification of the Eddy Diffusivity

Thus the Lagrangian and Eulerian (PV-derived) diffusivities agree within the errors over all slopes in the upper layer, but the Lagrangian diffusivities are consistently smaller than the Eulerian in the lower layer (Figure 7b), even though the Lagrangian and Eulerian PV fluxes match (Figure 5b). Why?

To obtain a relation between the two measures, we consider the Lagrangian eddy PV flux. We do this by rewriting the PV Equations 5a and 5b in Lagrangian form:

$$\frac{\mathrm{d}q_j}{\mathrm{d}t} = -Q_{jy} v_j - \delta_{j2}\mu\zeta_2, \tag{14}$$

where $Q_{jy} \equiv \partial Q_j/\partial y$ is the background PV gradient, $\zeta_2 \equiv \nabla^2\psi_2$ is the relative vorticity in the lower layer and δ_{jk} is the Kronecker delta. Note we absorb mean advection into the derivative in the upper layer (it has no bearing on what follows). Integrating (14) in time gives:

$$q_j(t) - q_j(0) = -Q_{jy}\left(y_j(t) - y_j(0)\right) - \delta_{j2}\mu\int_0^t \zeta_2(t')\,\mathrm{d}t'. \tag{15}$$

We multiply (15) by the meridional eddy velocity and average over all particles and then in time (over the last 100 days of each particle release as before) to get the Lagrangian eddy PV flux:

$$\left\langle v_j(t)q_j(t)\right\rangle_L = -Q_{jy}\left\langle v_j(t)\left[y_j(t) - y_j(0)\right]\right\rangle_L - \delta_{j2}\mu\int_0^t \left\langle v_j(t)\zeta_2(t')\right\rangle_L \mathrm{d}t'. \tag{16}$$

We have neglected the term $\left\langle v_j(t)q_j(0)\right\rangle_L$ on the assumption that the time-averaged eddy velocities are zero (no Stokes drift). Following Taylor (1921) and Equations 6a and 6e, we can rewrite (16) thus:

$$\left\langle v_j(t)q_j(t)\right\rangle_L = -\int_0^t \left[Q_{jy}\left\langle v_j(t)v_j(t')\right\rangle_L + \delta_{j2}\mu\left\langle v_j(t)\zeta_2(t')\right\rangle_L\right]\mathrm{d}t'. \tag{17}$$

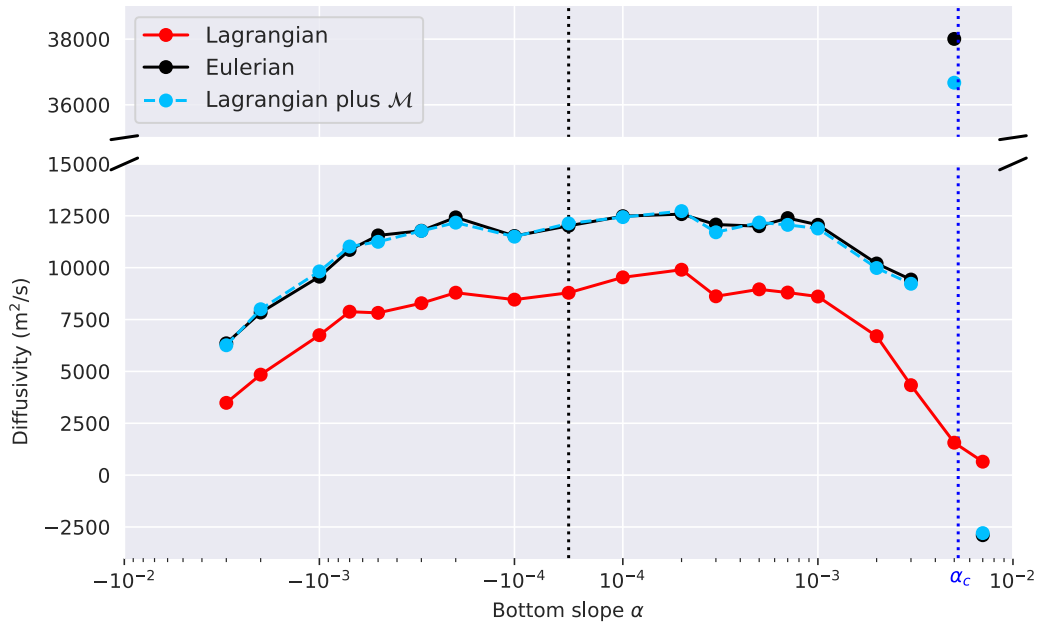

Figure 9. Lower layer Lagrangian and Eulerian cross-slope diffusivities as a function of the topographic slope, shown together with the sum of the Lagrangian diffusivity and the term $\mathcal{M}$ (Equation 19).

The left-hand side of (17) is the Lagrangian eddy PV flux, which is equal to the Eulerian eddy PV flux (Figure 5), and thus to the Eulerian diffusivity $\mathcal{K}_E$ times the PV gradient (Equation 7). In the first term on the right-hand side of (17) we recognize the Lagrangian diffusivity, $\mathcal{K}_L$ (Equation 6d). So we can rewrite (17) as follows:

$$\mathcal{K}_{E,j} = \mathcal{K}_{L,j} + \delta_{j2} \underbrace{\int_0^t \frac{\mu}{Q_{jy}} \langle v_j(t)\zeta_2(t')\rangle_L \mathrm{d}t'}_{\mathcal{M}}. \tag{18}$$

Equation 18 shows that the Eulerian PV flux has two contributions, one from Lagrangian dispersion and one from bottom friction. Thus the Eulerian and Lagrangian diffusivities should agree in the upper layer but differ in the lower. In the latter case the diffusivities are offset by a term $\mathcal{M}$ that depends on the frictional strength, the bottom slope, and the correlation between the lower layer relative vorticity and cross-slope velocity:

$$\mathcal{M} \equiv \frac{\mu}{-F_2 U + f_0 \alpha / H_2} \int_0^t \langle v_2(t)\zeta_2(t')\rangle_L \mathrm{d}t'. \tag{19}$$

As such, the Eulerian diffusivity differs greatly from the Lagrangian near the critical slope, where the denominator in (19) vanishes. This is a direct result of bottom friction. In the inviscid case ($\mu = 0$), the Eulerian and Lagrangian diffusivities would match in both layers.

How does one evaluate $\mathcal{M}$? This can be seen from Equation 17. The Lagrangian diffusivity is proportional to the autocorrelation of the Lagrangian velocity, as noted above. The friction term is similar but involves the correlation between the velocity and the relative vorticity on the parcel. To evaluate the first term, we integrate to a time, t, at which the integral has converged (LaCasce et al., 2014). This suggests the velocity-vorticity integral should be handled the same way.

Thus we compute $\mathcal{M}$ for all particle releases. We interpolate v_2 and ζ_2 to the particle locations at every time step, compute the biased covariance between them and then integrate in time. We average over the last 100 days of each particle release to obtain the asymptotic value of the integral, as done before.

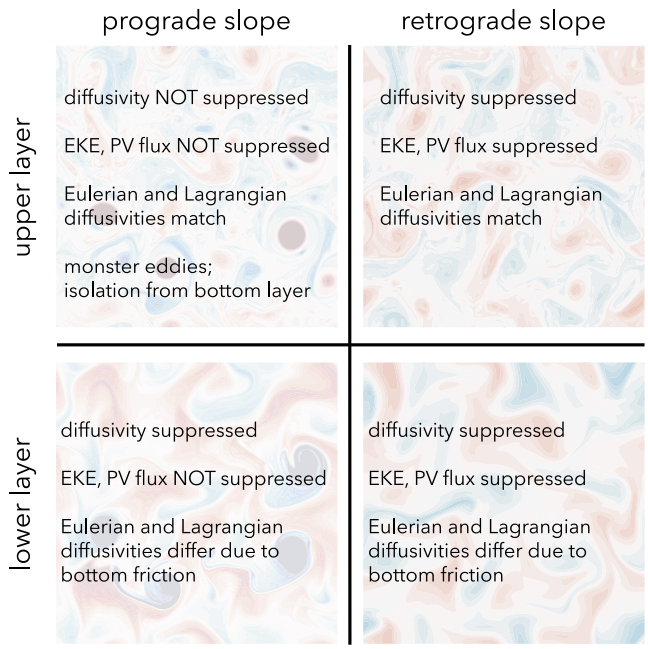

Figure 10. Summary of the findings from this study regarding the effects of topographic slopes compared to the flat bottom case, for both the upper and lower layer.

The result is shown in Figure 9. Indeed, $\mathcal{K}_{L,2} + \mathcal{M}$ matches $\mathcal{K}_{E,2}$ for all slopes, even close to and beyond the critical slope. In the latter case the frictional contribution explains why the Eulerian diffusivity becomes negative. For slopes $\alpha < \alpha_c$, the Eulerian diffusivity exceeds the Lagrangian diffusivity, meaning $\mathcal{M}$ is positive; since $Q_{2y} < 0$, this means that the correlation between v_2 and ζ_2 is, on average, negative. For $\alpha > \alpha_c$, this is the other way around. So anticyclonic eddies ($\zeta_2 < 0$) tend to drift in the opposite direction of Q_{2y}, and cyclonic eddies in the same direction. Hence, anticyclones tend to drift downslope for $\alpha < 0$ and $\alpha > \alpha_c$, and upslope for $0 < \alpha < \alpha_c$. The movement of the eddies is thus influenced not only by the topographic slope, but by the total PV gradient in the lower layer.

4. Summary and Discussion

4.1. Summary

A graphical summary of the results is shown in Figure 10. We showed that the effect of topographic slopes on layer-wise eddy diffusivity is asymmetric between prograde and retrograde slopes, in agreement with results for the diffusivity based on the eddy streamfunction (Deng & Wang, 2024). Moreover, there is asymmetry between the upper and the lower layer, and between Lagrangian and Eulerian diffusivities.

Retrograde (positive) slopes suppress the eddy diffusivity compared to flat or weak slopes in both the upper and the lower layer (Figure 7), in line with expectations based on PV suppression theory. Notably, when there is no PV gradient in the lower layer, PV suppression theory predicts no suppression of cross-slope fluxes. The lower layer flux, however, still decreases monotonically for positive slopes, as does the Lagrangian diffusivity. This suggests that it is the topographic PV gradient rather than the layer-wise PV gradient that determines the PV suppression, and the Lagrangian diffusivity captures the suppression in both layers.

Prograde (negative) slopes suppress the diffusivity in the lower layer, but not in the upper layer. With strong prograde slopes, monster eddies form: highly coherent, long-lived, surface-trapped vortices with very high EKE. The formation mechanism of the monster eddies remains a puzzle.

Lagrangian and Eulerian diffusivity values are equal in the upper layer for all slopes, but not in the lower layer. We derived a new relation between the two diffusivities, demonstrating that it is bottom friction that causes the difference in the lower layer. It is thus important to consider the joint effects of topographic slopes and bottom friction to understand QG turbulence.

4.2. Linear Stability Properties

Asymmetric effects of topographic slopes are also seen in the linear stability properties of the 2LQG model. The topographic PV gradients suppress the growth rates, but retrograde slopes do so more strongly than prograde slopes, as shown previously by Blumsack and Gierasch (1972) and others. In the frictionless case, retrograde slopes beyond the critical slope even suppress all baroclinic instability (Charney & Stern, 1962; Pavec et al., 2005; Pedlosky, 1963, 1964; Steinsaltz, 1987; Tang, 1976).

However, the situation changes with bottom friction. Topography and bottom friction jointly influence linear stability properties and, if strong enough, friction can dominate the response, effectively negating the asymmetric slope influence (Sterl et al., 2025). Moreover, the flow can be unstable over supercritical slopes, which explains why we observed turbulence in those cases as well.

In our simulations, we employed strong bottom friction, but the growth rate of the most unstable mode is still asymmetric between positive and negative slopes. Using the model of Sterl et al. (2025) and the present parameters, we obtain the growth rates shown in Figure 11. These are almost constant for slopes less than 10^{-3} but decrease for steeper slopes, and they decrease more dramatically for positive slopes.

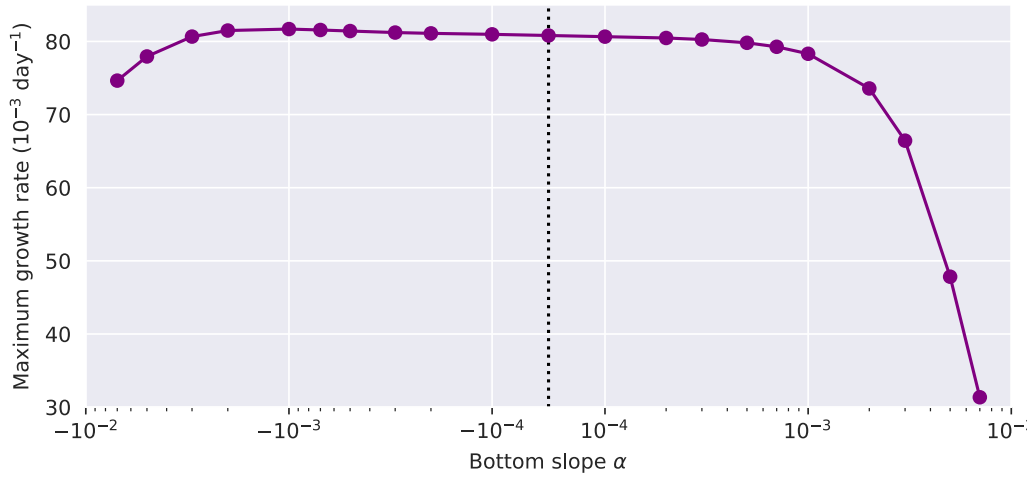

Figure 11. The growth rate of the most unstable mode as a function of the topographic slope, using the stability model of Sterl et al. (2025) with the model parameters used in our simulations.

This is a likely explanation then for the observed asymmetry on the diffusivities. Instability is suppressed with strong slopes and hence the energy levels are lower, particularly if the slope is positive (Figure 5d). As noted, the upper layer EKE and diffusivities are less affected over negative slopes, because of the formation of the monster eddies.

4.3. Monster Eddies

The coherent, long-lived eddies which form over strong negative slopes (Figures 1 and 4), are surface-trapped and therefore unaffected by the topographic slope or bottom friction. The imprint of these "monster eddies" manifests in the lower layer PV flux as well, through the Bretherton relation (8). Previous studies reported similar vortices in 2LQG flat bottom β-plane simulations. Berloff et al. (2011) studied zonal flows (as here) and found the strong vortices form with a westward mean flow but not an eastward one. Arbic and Flierl (2004b) found strong surface vortices with various orientations of the mean flow: with meridional flows, westward zonal flows and flows oriented slightly east of south (or north). Moreover, they formed only when β was nonzero. They also found strong vortices when planetary β was restricted to the lower layer, as is the case here with topographic β. Although planetary and topographic PV have distinct effects on geostrophic turbulence in the 2LQG model (Deng & Wang, 2024), the formation of monster eddies appears to be common in both.

It is likely the eddies reflect a linear unstable mode when the mean flow has certain orientations to the slope or planetary β. Brink and Pedlosky (2020) examined the modes resulting from an unstable mean flow with a range of orientations over a linear bottom slope. The $n = 0$ mode is often bottom-intensified, but the $n = 1$ mode can be entirely surface-trapped under certain orientations. A similar mode likely exists in the present context with a strong prograde slope. Then the surface eddies would extract energy from the mean flow but would be undamped by bottom drag. As such, they could become very strong and persist for long periods of time. This could be checked by solving the full stability problem (i.e., for all modes), using the parameters employed here. We leave this for future work.

The calculation of Brink and Pedlosky (2020) was with continuous stratification. Hence monster eddies are likely to occur with continuous stratification as well. The key requirement is that the unstable mode is surface-trapped, and thus isolated from bottom drag.

If monster eddies occurred in the ocean, they could have substantial impact. They could enhance lateral transport over the entire water column, and provide a means for long range, advective transport. Their presence could also thwart estimating frictional drag from surface data, as pointed out by Arbic and Flierl (2004b). Thus it is worth studying under what conditions they would be expected to form.

4.4. Relation Between Lagrangian and Eulerian Diffusivities

We presented an analytical relation between the Lagrangian and Eulerian diffusivities (Equation 18). The two measures differ in the presence of friction, which alters the PV along a particle path. The simulations support the relation. The diffusivities match in the upper layer (Figure 7a), with minor differences only in the monster eddy runs (noting that particles trapped in monster eddies have been excluded from the analysis). This agreement was noted previously, by W. Zhang et al. (2020) and W. Zhang and Wolfe (2024) for a flat bottom β-plane case. To our knowledge, the difference in diffusivities in the presence of bottom friction has not been noticed previously. The focus in previous baroclinic turbulence studies has mostly been on vertical modes, and the baroclinic diffusivity in particular. The present results highlight the advantage of thinking in terms of layers instead, as friction affects the bottom layer but also affects all modes. Indeed, the flat bottom modes cease to be relevant in the presence of topography (LaCasce, 2017), which is another good reason to focus on layers.

The difference between the layer diffusivities stems from the fact that the particles are a passive tracer while PV is an active tracer. With friction, the PV is not conserved along a particle path and this impacts the deduced mixing. Without friction, the Lagrangian and PV-diagnosed diffusivities are the same, as in the upper layer here. A related question is how well eddy fluxes of other active tracers, such as temperature, capture Lagrangian diffusivities in the presence of non-conservative forcing. This could have implications for the representation of eddy-induced mixing in global ocean-climate models.

The difference between the diffusivities is proportional to the integral of the correlation between the lower layer cross-slope velocity and relative vorticity. For a positive slope below the critical slope this term is negative, indicating a preference for anti-cyclones to drift upslope. This is counter to the usual expectation for vortices over sloping bathymetry (Carnevale et al., 1988; Köhl, 2007; LaCasce et al., 2024; Solodoch et al., 2021). However, the latter applies in the absence of a mean flow. When the eddies are generated by baroclinic instability, as is the case here, the propagation changes. The difference could have consequences for the types of eddies one would expect to find in different regions.

Relation (18) also informs on how the present results would extend to N layers. Then frictional modification of the diffusivity would be expected only in the lowest layer, as PV would be conserved in the other layers. However, in practice this may not always be the case. If a model employs interfacial friction, e.g., the Eulerian flux would again be expected to differ. Similar arguments apply to continuous stratification. The Eulerian and Lagrangian diffusivities will agree as long as PV is exactly conserved in the interior, and would be expected to differ only on the boundaries (e.g., Haynes & McIntyre, 1990).

4.5. Linear Versus Quadratic Bottom Friction

In the present study, we used linear bottom friction with an inverse frictional timescale of roughly 4 days, which is a large value for the ocean (Arbic & Flierl, 2004a). We opted for this to prevent the inverse energy cascade from reaching the domain scale. It would be informative to do the experiments with different frictional strengths μ. From Equation 18 we see that the Eulerian PV diffusivity scales linearly with μ, but since friction affects the isotropy and strength of the eddy field, it may also influence the velocity autocorrelation and the velocity-vorticity correlation.

Moreover, linear and quadratic bottom friction impact the diffusivity in different ways (Chang & Held, 2019; Chen, 2023; Gallet & Ferrari, 2020, 2021). Most relevant to our study, Deng and Wang (2024) showed that the dependence of eddy diffusivity on topographic slope varies with the strength of the quadratic bottom friction. Future work should build on these results to explore the role of linear and quadratic bottom friction in combination with topographic slopes and the impact on the layer-wise eddy diffusivities.

Conflict of Interest

The authors declare no conflicts of interest relevant to this study.

Availability Statement

Code for reproducing the results is available at https://doi.org/10.5281/zenodo.18612653 (Sterl, 2026).

Acknowledgments
MFS and SG were funded by the UU-NIOZ project "The intermittency of large-scale ocean mixing" (project number NZ4543.3). AP was supported with Institutional Funding at the National Oceanography Centre, UK. JHL was supported by the Research Council of Norway (RCN) project The Rough Ocean (project number 302743). MLJB was funded by the program of the Netherlands Earth System Science Centre (NESSC), financially supported by the Ministry of Education, Culture and Science (OCW, Grant 024.002.001). We thank Matthew Lobo, Michael Denes and Michal Shaham for insightful discussions. We also thank two anonymous reviewers, whose feedback greatly helped improve the article.

References

Abernathey, R., & Haller, G. (2018). Transport by lagrangian vortices in the eastern Pacific. *Journal of Physical Oceanography*, *48*(3), 667–685. https://doi.org/10.1175/JPO-D-17-0102.1

Arbic, B. K., & Flierl, G. R. (2004a). Baroclinically unstable geostrophic turbulence in the limits of strong and weak bottom ekman friction: Application to midocean eddies. *Journal of Physical Oceanography*, *34*(10), 2257–2273. https://doi.org/10.1175/1520-0485(2004)034<2257:BUGTIT>2.0.CO;2

Arbic, B. K., & Flierl, G. R. (2004b). Effects of mean flow direction on energy, isotropy, and coherence of baroclinically unstable beta-plane geostrophic turbulence. *Journal of Physical Oceanography*, *34*(1), 77–93. https://doi.org/10.1175/1520-0485(2004)034<0077:EOMFDO>2.0.CO;2

Balwada, D., Speer, K. G., LaCasce, J. H., Owens, W. B., Marshall, J., & Ferrari, R. (2016). Circulation and stirring in the southeast Pacific Ocean and the Scotia Sea sectors of the Antarctic circumpolar current. *Journal of Physical Oceanography*, *46*(7), 2005–2027. https://doi.org/10.1175/JPO-D-15-0207.1

Berloff, P., Karabasov, S., Farrar, J. T., & Kamenkovich, I. (2011). On latency of multiple zonal jets in the oceans. *Journal of Fluid Mechanics*, *686*, 534–567. https://doi.org/10.1017/jfm.2011.345

Blumsack, S. L., & Gierasch, P. J. (1972). Mars: The effects of topography on baroclinic instability. *Journal of the Atmospheric Sciences*, *29*(6), 1081–1089. https://doi.org/10.1175/1520-0469(1972)029<1081:MTEOTO>2.0.CO;2

Bretherton, F. P. (1966). Baroclinic instability and the short wavelength cut-off in terms of potential vorticity. *Quarterly Journal of the Royal Meteorological Society*, *92*(393), 335–345. https://doi.org/10.1002/qj.49709239303

Brink, K. H. (2012). Baroclinic instability of an idealized tidal mixing front. *Journal of Marine Research*, *70*(4), 661–688. https://doi.org/10.1357/002224012805262716

Brink, K. H. (2016). Continental shelf baroclinic instability. Part I: Relaxation from upwelling or downwelling. *Journal of Physical Oceanography*, *46*(2), 551–568. https://doi.org/10.1175/JPO-D-15-0047.1

Brink, K. H., & Cherian, D. A. (2013). Instability of an idealized tidal mixing front: Symmetric instabilities and frictional effects. *Journal of Marine Research*, *71*(6), 425–450. https://doi.org/10.1357/002224013812587582

Brink, K. H., & Pedlosky, J. (2020). The structure of baroclinic modes in the presence of baroclinic mean flow. *Journal of Physical Oceanography*, *50*(1), 239–253. https://doi.org/10.1175/JPO-D-19-0123.1

Carnevale, G. F., Vallis, G. K., Purini, R., & Briscolini, M. (1988). Propagation of barotropic modons over topography. *Geophysical and Astrophysical Fluid Dynamics*, *41*(1–2), 45–101. https://doi.org/10.1080/03091928808208831

Chang, C.-Y., & Held, I. M. (2019). The control of surface friction on the scales of baroclinic eddies in a homogeneous quasigeostrophic two-layer model. *Journal of the Atmospheric Sciences*, *76*(6), 1627–1643. https://doi.org/10.1175/JAS-D-18-0333.1

Chang, C.-Y., & Held, I. M. (2021). The parameter dependence of eddy heat flux in a homogeneous quasigeostrophic two-layer model on a β plane with quadratic friction. *Journal of the Atmospheric Sciences*, *78*(1), 97–106. https://doi.org/10.1175/JAS-D-20-0145.1

Chapman, C., & Sallée, J.-B. (2017). Isopycnal mixing suppression by the Antarctic Circumpolar current and the Southern Ocean meridional overturning circulation. *Journal of Physical Oceanography*, *47*(8), 2023–2045. https://doi.org/10.1175/JPO-D-16-0263.1

Charney, J. G., & Stern, M. E. (1962). On the stability of internal baroclinic jets in a rotating atmosphere. *Journal of the Atmospheric Sciences*, *19*(2), 159–172. https://doi.org/10.1175/1520-0469(1962)019<0159:OTSOIB>2.0.CO;2

Chen, S.-N. (2023). Revisiting the baroclinic eddy scalings in two-layer, quasigeostrophic turbulence: Effects of partial barotropization. *Journal of Physical Oceanography*, *53*(3), 891–913. https://doi.org/10.1175/JPO-D-22-0102.1

Chiswell, S. M. (2013). Lagrangian time scales and eddy diffusivity at 1000 m compared to the surface in the south Pacific and Indian oceans. *Journal of Physical Oceanography*, *43*(12), 2718–2732. https://doi.org/10.1175/JPO-D-13-044.1

Chouksey, A., Griesel, A., Chouksey, M., & Eden, C. (2022). Changes in global ocean circulation due to isopycnal diffusion. *Journal of Physical Oceanography*, *52*(9), 2219–2235. https://doi.org/10.1175/JPO-D-21-0205.1

Cole, S. T., Wortham, C., Kunze, E., & Owens, W. B. (2015). Eddy stirring and horizontal diffusivity from argo float observations: Geographic and depth variability. *Geophysical Research Letters*, *42*(10), 3989–3997. https://doi.org/10.1002/2015GL063827

Colin de Verdiere, A. (1983). Lagrangian eddy statistics from surface drifters in the eastern north Atlantic. *Journal of Marine Research*, *41*(3), 375–398. https://doi.org/10.1357/002224083788519713

Constantinou, N., Wagner, G., Siegelman, L., Pearson, B., & Palóczy, A. (2021). GeophysicalFlows.jl: Solvers for geophysical fluid dynamics problems in periodic domains on CPUs and GPUs. *Journal of Open Source Software*, *6*(60), 3053. https://doi.org/10.21105/joss.03053

Davis, R. E. (1987). Modeling eddy transport of passive tracers. *Journal of Marine Research*, *45*(3), 635–666. https://doi.org/10.1357/002224087788326803

Davis, R. E. (1991). Observing the general circulation with floats. *Deep-Sea Research, Part A: Oceanographic Research Papers*, *38*, S531–S571. https://doi.org/10.1016/S0198-0149(12)80023-9

De La Lama, M. S., LaCasce, J. H., & Fuhr, H. K. (2016). The vertical structure of ocean eddies. *Dynamics and Statistics of the Climate System*, dzw001. https://doi.org/10.1093/climsys/dzw001

Delandmeter, P., & van Sebille, E. (2019). The parcels v2.0 lagrangian framework: New field interpolation schemes. *Geoscientific Model Development*, *12*(8), 3571–3584. https://doi.org/10.5194/gmd-12-3571-2019

Denes, M. C., Froyland, G., & Keating, S. R. (2022). Persistence and material coherence of a mesoscale ocean eddy. *Physical Review Fluids*, *7*(3), 034501. https://doi.org/10.1103/PhysRevFluids.7.034501

Deng, P., & Wang, Y. (2024). Distinct impacts of topographic versus planetary PV gradients on baroclinic turbulence. *Journal of Physical Oceanography*, *54*(10), 2205–2231. https://doi.org/10.1175/JPO-D-24-0014.1

Dettling, N., Losch, M., Pollmann, F., & Kanzow, T. (2024). Toward parameterizing eddy-mediated transport of warm deep water across the Weddell Sea Continental slope. *Journal of Physical Oceanography*, *54*(8), 1675–1690. https://doi.org/10.1175/JPO-D-23-0215.1

Dettling, N., Nakayama, Y., Mensah, V., & Losch, M. (2025). A topography-aware eddy parameterization improves warm water transport across the cape darnley Continental slope. *Journal of Advances in Modeling Earth Systems*, *17*(8), e2025MS005115. https://doi.org/10.1029/2025MS005115

Eden, C., & Greatbatch, R. J. (2008). Towards a mesoscale eddy closure. *Ocean Modelling*, *20*(3), 223–239. https://doi.org/10.1016/j.ocemod.2007.09.002

Feng, L., Liu, C., Köhl, A., Stammer, D., & Wang, F. (2021). Four types of baroclinic instability waves in the global oceans and the implications for the vertical structure of mesoscale eddies. *Journal of Geophysical Research: Oceans*, *126*(3), e2020JC016966. https://doi.org/10.1029/2020JC016966

Ferrari, R., & Nikurashin, M. (2010). Suppression of eddy diffusivity across jets in the Southern Ocean. *Journal of Physical Oceanography*, *40*(7), 1501–1519. https://doi.org/10.1175/2010JPO4278.1

Ferrari, R., & Wunsch, C. (2009). Ocean circulation kinetic energy: Reservoirs, sources, and sinks. *Annual Review of Fluid Mechanics*, *41*(1), 253–282. https://doi.org/10.1146/annurev.fluid.40.111406.102139

Flierl, G. R. (1978). Models of vertical structure and the calibration of two-layer models. *Dynamics of Atmospheres and Oceans*, *2*(4), 341–381. https://doi.org/10.1016/0377-0265(78)90002-7

Fox-Kemper, B., Adcroft, A., Böning, C. W., Chassignet, E. P., Curchitser, E., Danabasoglu, G., et al. (2019). Challenges and prospects in ocean circulation models. *Frontiers in Marine Science*, *6*, 65. https://doi.org/10.3389/fmars.2019.00065

Freeland, H. J., Rhines, P. B., & Rossby, T. (1975). Statistical observations of the trajectories of neutrally buoyant floats in the north Atlantic. *Journal of Marine Research*, *33*, 383–404.

Frenger, I., Münnich, M., Gruber, N., & Knutti, R. (2015). Southern Ocean eddy phenomenology. *Journal of Geophysical Research: Oceans*, *120*(11), 7413–7449. https://doi.org/10.1002/2015JC011047

Gallet, B., & Ferrari, R. (2020). The vortex gas scaling regime of baroclinic turbulence. *Proceedings of the National Academy of Sciences*, *117*(9), 4491–4497. https://doi.org/10.1073/pnas.1916272117

Gallet, B., & Ferrari, R. (2021). A quantitative scaling theory for meridional heat transport in planetary atmospheres and oceans. *AGU Advances*, *2*(3), e2020AV000362. https://doi.org/10.1029/2020AV000362

Gent, P. R., & McWilliams, J. C. (1990). Isopycnal mixing in ocean circulation models. *Journal of Physical Oceanography*, *20*(1), 150–155. https://doi.org/10.1175/1520-0485(1990)020<0150:IMIOCM>2.0.CO;2

Gill, A., Green, J., & Simmons, A. (1974). Energy partition in the large-scale ocean circulation and the production of mid-ocean eddies. *Deep-Sea Research and Oceanographic Abstracts*, *21*(7), 499–528. https://doi.org/10.1016/0011-7471(74)90010-2

Gnanadesikan, A., Bianchi, D., & Pradal, M.-A. (2013). Critical role for mesoscale eddy diffusion in supplying oxygen to hypoxic ocean waters. *Geophysical Research Letters*, *40*(19), 5194–5198. https://doi.org/10.1002/grl.50998

Gnanadesikan, A., Pradal, M.-A., & Abernathey, R. (2015). Isopycnal mixing by mesoscale eddies significantly impacts Oceanic anthropogenic carbon uptake. *Geophysical Research Letters*, *42*(11), 4249–4255. https://doi.org/10.1002/2015GL064100

Griesel, A., Eden, C., Koopmann, N., & Yulaeva, E. (2015). Comparing isopycnal eddy diffusivities in the Southern Ocean with predictions from linear theory. *Ocean Modelling*, *94*, 33–45. https://doi.org/10.1016/j.ocemod.2015.08.001

Griesel, A., Gille, S. T., Sprintall, J., McClean, J. L., Lacasce, J. H., & Maltrud, M. E. (2010). Isopycnal diffusivities in the antarctic circumpolar Current inferred from Lagrangian floats in an eddying model. *Journal of Geophysical Research*, *115*(6). https://doi.org/10.1029/2009JC005821

Groeskamp, S., LaCasce, J. H., McDougall, T. J., & Rogé, M. (2020). Full-Depth global estimates of ocean mesoscale eddy mixing from observations and theory. *Geophysical Research Letters*, *47*(18), 1–12. https://doi.org/10.1029/2020GL089425

Groeskamp, S., Sloyan, B. M., Zika, J. D., & McDougall, T. J. (2017). Mixing inferred from an ocean climatology and surface fluxes. *Journal of Physical Oceanography*, *47*(3), 667–687. https://doi.org/10.1175/JPO-D-16-0125.1

Hallberg, R. (2013). Using a resolution function to regulate parameterizations of Oceanic mesoscale eddy effects. *Ocean Modelling*, *72*, 92–103. https://doi.org/10.1016/j.ocemod.2013.08.007

Harrison, C. S., Long, M. C., Lovenduski, N. S., & Moore, J. K. (2018). Mesoscale effects on carbon export: A global perspective. *Global Biogeochemical Cycles*, *32*(4), 680–703. https://doi.org/10.1002/2017GB005751

Haynes, P. H., & McIntyre, M. E. (1990). On the conservation and impermeability theorems for potential vorticity. *Journal of the Atmospheric Sciences*, *47*(16), 2021–2031. https://doi.org/10.1175/1520-0469(1990)047<2021:OTCAIT>2.0.CO;2

Hewitt, H. T., Bell, M. J., Chassignet, E. P., Czaja, A., Ferreira, D., Griffies, S. M., et al. (2017). Will high-resolution global ocean models benefit coupled predictions on short-range to climate timescales? *Ocean Modelling*, *120*, 120–136. https://doi.org/10.1016/j.ocemod.2017.11.002

Hewitt, H. T., Roberts, M., Mathiot, P., Biastoch, A., Blockley, E., Chassignet, E. P., et al. (2020). Resolving and parameterising the ocean mesoscale in Earth system models. *Current Climate Change Reports*, *6*(4), 137–152. https://doi.org/10.1007/s40641-020-00164-w

Holmes, R. M., Groeskamp, S., Stewart, K. D., & McDougall, T. J. (2022). Sensitivity of a coarse-resolution global ocean model to a spatially variable neutral diffusivity. *Journal of Advances in Modeling Earth Systems*, *14*(3), e2021MS002914. https://doi.org/10.1029/2021MS002914

Isachsen, P. E. (2011). Baroclinic instability and eddy tracer transport across sloping bottom topography: How well does a modified eady model do in primitive equation simulations? *Ocean Modelling*, *39*(1–2), 183–199. https://doi.org/10.1016/j.ocemod.2010.09.007

Jansen, M. F., Adcroft, A. J., Hallberg, R., & Held, I. M. (2015). Parameterization of eddy fluxes based on a mesoscale energy budget. *Ocean Modelling*, *92*, 28–41. https://doi.org/10.1016/j.ocemod.2015.05.007

Jansen, M. F., & Held, I. M. (2014). Parameterizing subgrid-scale eddy effects using energetically consistent backscatter. *Ocean Modelling*, *80*, 36–48. https://doi.org/10.1016/j.ocemod.2014.06.002

Jones, C. S., & Abernathey, R. P. (2019). Isopycnal mixing controls deep ocean ventilation. *Geophysical Research Letters*, *46*(22), 13144–13151. https://doi.org/10.1029/2019GL085208

Kjellsson, J., & Zanna, L. (2017). The impact of horizontal resolution on energy transfers in global ocean models. *Fluids*, *2*(3), 45. https://doi.org/10.3390/fluids2030045

Klocker, A., Ferrari, R., & LaCasce, J. H. (2012a). Estimating suppression of eddy mixing by mean flows. *Journal of Physical Oceanography*, *42*(9), 1566–1576. https://doi.org/10.1175/JPO-D-11-0205.1

Klocker, A., Ferrari, R., Lacasce, J. H., & Merrifield, S. T. (2012b). Reconciling float-based and tracer-based estimates of lateral diffusivities. *Journal of Marine Research*, *70*(4), 569–602. https://doi.org/10.1357/002224012805262743

Köhl, A. (2007). Generation and stability of a quasi-permanent vortex in the lofoten basin. *Journal of Physical Oceanography*, *37*(11), 2637–2651. https://doi.org/10.1175/2007JPO3694.1

Kong, H., & Jansen, M. F. (2017). The eddy diffusivity in barotropic β-plane turbulence. *Fluids*, *2*(4), 54. https://doi.org/10.3390/fluids2040054

Kraichnan, R. H. (1967). Inertial ranges in two-dimensional turbulence. *The Physics of Fluids*, *10*(7), 1417–1423. https://doi.org/10.1063/1.1762301

LaCasce, J. H. (2000). Floats and f/H. *Journal of Marine Research*, *58*(1), 61–95. https://doi.org/10.1357/002224000321511205

LaCasce, J. H. (2008a). Statistics from Lagrangian observations. *Progress in Oceanography*, *77*(1), 1–29. https://doi.org/10.1016/j.pocean.2008.02.002

LaCasce, J. H. (2008b). The vortex merger rate in freely decaying, two-dimensional turbulence. *Physics of Fluids*, *20*(8), 085102. https://doi.org/10.1063/1.2957020

LaCasce, J. H. (2017). The prevalence of Oceanic surface modes. *Geophysical Research Letters*, *44*(21), 11097–11105. https://doi.org/10.1002/2017GL075430

LaCasce, J. H., Ferrari, R., Marshall, J., Tulloch, R., Balwada, D., & Speer, K. (2014). Float-derived isopycnal diffusivities in the DIMES experiment. *Journal of Physical Oceanography*, *44*(2), 764–780. https://doi.org/10.1175/JPO-D-13-0175.1

LaCasce, J. H., & Groeskamp, S. (2020). Baroclinic modes over rough bathymetry and the surface deformation radius. *Journal of Physical Oceanography*, *50*(10), 2835–2847. https://doi.org/10.1175/JPO-D-20-0055.1

LaCasce, J. H., Palóczy, A., & Trodahl, M. (2024). Vortices over bathymetry. *Journal of Fluid Mechanics*, *979*, A32. https://doi.org/10.1017/jfm.2023.1084

Larichev, V., & Held, I. (1995). Eddy amplitudes and fluxes in a homogeneous model of fully developed baroclinic instability. *Journal of Physical Oceanography*, *25*(10), 2285–2297. https://doi.org/10.1175/1520-0485(1995)025<2285:eaafia>2.0.co;2

Lee, M.-M., Nurser, A. J. G., Coward, A. C., & de Cuevas, B. A. (2007). Eddy advective and diffusive transports of heat and salt in the Southern Ocean. *Journal of Physical Oceanography*, *37*(5), 1376–1393. https://doi.org/10.1175/JPO3057.1

Marshall, J., Shuckburgh, E., Jones, H., & Hill, C. (2006). Estimates and implications of surface eddy diffusivity in the Southern Ocean derived from tracer transport. *Journal of Physical Oceanography*, *36*(9), 1806–1821. https://doi.org/10.1175/jpo2949.1

Nakamura, N., & Zhu, D. (2010). Formation of jets through mixing and forcing of potential vorticity: Analysis and parameterization of beta-plane turbulence. *Journal of the Atmospheric Sciences*, *67*(9), 2717–2733. https://doi.org/10.1175/2009JAS3159.1

Naveira Garabato, A. C., Ferrari, R., & Polzin, K. L. (2011). Eddy stirring in the Southern Ocean. *Journal of Geophysical Research*, *116*(9), C09019. https://doi.org/10.1029/2010JC006818

Ni, Q., Zhai, X., LaCasce, J. H., Chen, D., & Marshall, D. P. (2023). Full-depth eddy kinetic energy in the global ocean estimated from altimeter and argo observations. *Geophysical Research Letters*, *50*(15), e2023GL103114. https://doi.org/10.1029/2023GL103114

Nummelin, A., & Isachsen, P. E. (2024). Parameterizing mesoscale eddy buoyancy transport over sloping topography. *Journal of Advances in Modeling Earth Systems*, *16*(3), e2023MS003806. https://doi.org/10.1029/2023MS003806

O'Dwyer, J., Williams, R. G., LaCasce, J. H., & Speer, K. G. (2000). Does the potential vorticity distribution constrain the spreading of floats in the north Atlantic? *Journal of Physical Oceanography*, *30*(4), 721–732. https://doi.org/10.1175/1520-0485(2000)030<0721:DTPVDC>2.0.CO;2

Oelerich, R., Gülk, B., Dräger-Dietel, J., & Griesel, A. (2025). An estimate of the eddy diffusivity tensor from observed and simulated Lagrangian trajectories in the Benguela upwelling system. *Ocean Science*, *21*, 727–747. https://doi.org/10.5194/egusphere-2024-2806

Pavec, M., Carton, X., & Swaters, G. (2005). Baroclinic instability of frontal geostrophic currents over a slope. *Journal of Physical Oceanography*, *35*(5), 911–918. https://doi.org/10.1175/JPO2718.1

Pedlosky, J. (1963). Baroclinic instability in two layer systems. *Tellus*, *15*(1), 20–25. https://doi.org/10.1111/j.2153-3490.1963.tb01359.x

Pedlosky, J. (1964). The stability of currents in the atmosphere and the ocean: Part I. *Journal of the Atmospheric Sciences*, *21*(2), 201–219. https://doi.org/10.1175/1520-0469(1964)021<0201:TSOCIT>2.0.CO;2

Pedlosky, J. (1987). *Geophysical fluid dynamics*. Springer.

Phillips, N. A. (1951). A simple three-dimensional model for the study of large-scale extratropical flow patterns. *Journal of Meteorology*, *8*(6), 381–394. https://doi.org/10.1175/1520-0469(1951)008<0381:ASTDMF>2.0.CO;2

Phillips, N. A. (1954). Energy transformations and meridional circulations associated with simple baroclinic waves in a two-level, quasi-geostrophic model. *Tellus*, *6*(3), 273–286. https://doi.org/10.1111/j.2153-3490.1954.tb01123.x

Pradal, M.-A., & Gnanadesikan, A. (2014). How does the redi parameter for mesoscale mixing impact global climate in an Earth system model? *Journal of Advances in Modeling Earth Systems*, *6*(3), 586–601. https://doi.org/10.1002/2013MS000273

Pudig, M. P., & Smith, K. S. (2025). Baroclinic turbulence above rough topography: The vortex gas and topographic turbulence regimes. *Journal of Physical Oceanography*, *55*(5), 611–630. https://doi.org/10.1175/JPO-D-24-0110.1

Roach, C. J., Balwada, D., & Speer, K. (2018). Global observations of horizontal mixing from argo float and surface drifter trajectories. *Journal of Geophysical Research: Oceans*, *123*(7), 4560–4575. https://doi.org/10.1029/2018JC013750

Robinson, A. R., & McWilliams, J. C. (1974). The baroclinic instability of the open ocean. *Journal of Physical Oceanography*, *4*(3), 281–294. https://doi.org/10.1175/1520-0485(1974)004<0281:TBIOTO>2.0.CO;2

Ruan, X., Couespel, D., Lévy, M., Li, J., Mak, J., & Wang, Y. (2023). Combined physical and biogeochemical assessment of mesoscale eddy parameterisations in ocean models: Eddy induced advection at non-eddying resolutions. *Ocean Modelling*, *183*, 102204. https://doi.org/10.1016/j.ocemod.2023.102204

Rühs, S., Zhurbas, V., Koszalka, I. M., Durgadoo, J. V., & Biastoch, A. (2018). Eddy diffusivity estimates from lagrangian trajectories simulated with ocean models and surface Drifter Data—A case study for the greater agulhas system. *Journal of Physical Oceanography*, *48*(1), 175–196. https://doi.org/10.1175/JPO-D-17-0048.1

Rypina, I. I., Kamenkovich, I., Berloff, P., & Pratt, L. J. (2012). Eddy-induced particle dispersion in the near-surface north Atlantic. *Journal of Physical Oceanography*, *42*(12), 2206–2228. https://doi.org/10.1175/JPO-D-11-0191.1

Salmon, R. (1980). Baroclinic instability and geostrophic turbulence. *Geophysical and Astrophysical Fluid Dynamics*, *15*(1), 167–211. https://doi.org/10.1080/03091928008241178

Solodoch, A., Stewart, A. L., & McWilliams, J. C. (2021). Formation of anticyclones above topographic depressions. *Journal of Physical Oceanography*, *51*(1), 207–228. https://doi.org/10.1175/JPO-D-20-0150.1

Srinivasan, K., & Young, W. R. (2014). Reynolds stress and eddy diffusivity of ss-plane shear flow. *Journal of the Atmospheric Sciences*, *71*(6), 2169–2185. https://doi.org/10.1175/JAS-D-13-0246.1

Steinberg, J. M., Yankovsky, E., Cole, S. T., & Zanna, L. (2025). A landscape of mesoscale eddy vertical structure: The influence of bathymetric slope and roughness on kinetic energy. *Journal of Physical Oceanography*, *55*(11), 1987–2004. https://doi.org/10.1175/JPO-D-25-0044.1

Steinsaltz, D. (1987). Instability of baroclinic waves with bottom slope. *Journal of Physical Oceanography*, *17*(12), 2343–2350. https://doi.org/10.1175/1520-0485(1987)017<2343:IOBWWB>2.0.CO;2

Sterl, M. F. (2026). Two-layer slope simulations – Code [Software]. *Zenodo*. https://doi.org/10.5281/zenodo.18612653

Sterl, M. F., LaCasce, J. H., Groeskamp, S., Nummelin, A., Isachsen, P. E., & Baatsen, M. L. J. (2024). Suppression of mesoscale eddy mixing by topographic PV gradients. *Journal of Physical Oceanography*, *54*(5), 1089–1103. https://doi.org/10.1175/JPO-D-23-0142.1

Sterl, M. F., Palóczy, A., Groeskamp, S., Baatsen, M. L. J., LaCasce, J. H., & Isachsen, P. E. (2025). The joint effects of planetary beta, topography and friction on baroclinic instability in a two-layer quasi-geostrophic model. *Journal of Fluid Mechanics*, *1012*, A1. https://doi.org/10.1017/jfm.2025.10172

Tang, C.-M. (1976). The influence of meridionally sloping topography on baroclinic instability and its implications for macroclimate. *Journal of the Atmospheric Sciences*, *33*(4), 592–601. https://doi.org/10.1175/1520-0469(1976)033<0592:TIOMST>2.0.CO;2

Taylor, G. I. (1921). Diffusion by continuous movements. *Proceedings of the London Mathematical Society*, *20*(1), 196–211. https://doi.org/10.1112/plms/s2-20.1.196

Thompson, A. F., & Young, W. R. (2006). Scaling baroclinic eddy fluxes: Vortices and energy balance. *Journal of Physical Oceanography*, *36*(4), 720–738. https://doi.org/10.1175/JPO2874.1

Thompson, A. F., & Young, W. R. (2007). Two-layer baroclinic eddy heat fluxes: Zonal flows and energy balance. *Journal of the Atmospheric Sciences*, *64*(9), 3214–3231. https://doi.org/10.1175/JAS4000.1

Vallis, G. K. (2021). Turbulence theory: Imperfect, but necessary. *AGU Advances*, *2*(3), e2021AV000523. https://doi.org/10.1029/2021AV000523

Vallis, G. K., & Maltrud, M. E. (1993). Generation of mean flows and jets on a beta plane and over topography. *Journal of Physical Oceanography*, *23*(7), 1346–1362. https://doi.org/10.1175/1520-0485(1993)023<1346:gomfaj>2.0.co;2

Wang, Y., & Stewart, A. L. (2020). Scalings for eddy buoyancy transfer across continental slopes under retrograde winds. *Ocean Modelling*, *147*, 101579. https://doi.org/10.1016/j.ocemod.2020.101579

Wei, H., & Wang, Y. (2021). Full-Depth scalings for isopycnal eddy mixing across Continental slopes under upwelling-favorable winds. *Journal of Advances in Modeling Earth Systems*, *13*(6), 1–40. https://doi.org/10.1029/2021MS002498

Wei, H., Wang, Y., & Mak, J. (2024). Parameterizing eddy buoyancy fluxes across prograde shelf/slope fronts using a slope-aware GEOMETRIC closure. *Journal of Physical Oceanography*, *54*(2), 359–377. https://doi.org/10.1175/JPO-D-23-0152.1

Wei, H., Wang, Y., Stewart, A. L., & Mak, J. (2022). Scalings for eddy buoyancy fluxes across prograde shelf/slope fronts. *Journal of Advances in Modeling Earth Systems*, *14*(12), e2022MS003229. https://doi.org/10.1029/2022MS003229

Yankovsky, E., Zanna, L., & Smith, K. S. (2022). Influences of mesoscale ocean eddies on flow vertical structure in a resolution-based model hierarchy. *Journal of Advances in Modeling Earth Systems*, *14*(11), e2022MS003203. https://doi.org/10.1029/2022MS003203

Zhang, W., & Wolfe, C. L. P. (2022). On the vertical structure of Oceanic mesoscale tracer diffusivities. *Journal of Advances in Modeling Earth Systems*, *14*(6), e2021MS002891. https://doi.org/10.1029/2021MS002891

Zhang, W., & Wolfe, C. L. P. (2024). Inferring tracer diffusivity from coherent mesoscale eddies. *Journal of Advances in Modeling Earth Systems*, *16*(4), e2023MS004004. https://doi.org/10.1029/2023MS004004

Zhang, W., Wolfe, C. L. P., & Abernathey, R. (2020). Role of surface-layer coherent eddies in potential vorticity transport in quasigeostrophic turbulence driven by eastward shear. *Fluids*, *5*(1), 2. https://doi.org/10.3390/fluids5010002

Zhang, Y., & Vallis, G. K. (2013). Ocean heat uptake in eddying and non-eddying ocean circulation models in a warming climate. *Journal of Physical Oceanography*, *43*(10), 2211–2229. https://doi.org/10.1175/JPO-D-12-078.1

Zhurbas, V., Lyzhkov, D., & Kuzmina, N. (2014). Drifter-derived estimates of lateral eddy diffusivity in the world ocean with emphasis on the Indian Ocean and problems of parameterisation. *Deep Sea Research Part I: Oceanographic Research Papers*, *83*, 1–11. https://doi.org/10.1016/j.dsr.2013.09.001

Zhurbas, V., & Oh, I. S. (2003). Lateral diffusivity and Lagrangian scales in the Pacific Ocean as derived from drifter data. *Journal of Geophysical Research*, *108*(C5), 2002JC001596. https://doi.org/10.1029/2002JC001596

Zhurbas, V., & Oh, I. S. (2004). Drifter-derived maps of lateral diffusivity in the Pacific and Atlantic oceans in relation to surface circulation patterns. *Journal of Geophysical Research*, *109*(C5), 2003JC002241. https://doi.org/10.1029/2003JC002241

Zika, J. D., & McDougall, T. J. (2008). Vertical and lateral mixing processes deduced from the mediterranean water signature in the north Atlantic. *Journal of Physical Oceanography*, *38*(1), 164–176. https://doi.org/10.1175/2007JPO3507.1

Zika, J. D., McDougall, T. J., & Sloyan, B. M. (2010). Weak mixing in the eastern north Atlantic: An application of the tracer-contour inverse method. *Journal of Physical Oceanography*, *40*(8), 1881–1893. https://doi.org/10.1175/2010JPO4360.1